

THESIS

STRUCTURAL OPTIMIZATION OF 3D PRINTED HDYROXYAPATITE SCAFFOLDS

Submitted by

Nelson D. Isaacson

School of Advanced Materials Discovery

In partial fulfillment of the requirements

For the Degree of Master of Science

Colorado State University

Fort Collins, Colorado

Summer 2021

Master's Committee:

Advisor: David Prawel
Susan James
Bernard Séguin

Copyright by Nelson David Isaacson 2021

All Rights Reserved

ABSTRACT

STRUCTURAL OPTIMIZATION OF 3D PRINTED HYDROXYAPATITE SCAFFOLDS

Poor healing of critically sized bone defects affects 1.5 million Americans per year and results in more than \$1 billion in treatment and therapy cost. Treatment options remain limited and often lead to reoperations, clinical complications, poor functional outcomes, and limb loss, making this one of the biggest challenges in orthopedic medicine, resulting in significant personal and economic cost. Healing strategies using autografts, allografts and xenografts are limited by shortage of available tissue and failure to heal, with complication rates of 50% from delayed or non-union, 30% from allograft fracture, and 15% from infection. Decades of research has been dedicated to solving this problem using a wide variety of bone regeneration techniques. Tissue engineered solutions have emerged that deploy biodegradable, osteoconductive scaffolds to provide structural support and osteoinductive stimulus, with suitable porosity to enable nutrient and waste exchange and angiogenesis. Promising calcium phosphate biomaterials like hydroxyapatite (HAp) and β -tricalcium phosphate are widely studied for bone regeneration scaffolds due to their excellent bioactivity (osteoinductivity, osteoconductivity and osseointegration), mineral composition and tunable degradation rates.

Advanced scaffold topologies such as a type of triply periodic minimal surface (TPMS) structure called gyroids are yielding scaffolds that are stiffer and stronger than traditional rectilinear scaffold topologies. Gyroids are ideal candidates for scaffold designs due to their relatively high mechanical energy absorption and robustness, interconnected internal porous structure, scalable unit cell topology, and smooth internal surfaces with relatively high surface area per volume.

In our study, a method of layer-wise, photopolymerized viscous extrusion, a type of additive manufacturing, was used to fabricate HAp gyroid scaffolds with 60%, 70% and 80% porosities. Our study is the first to use this method to produce and evaluate calcium-phosphate-based scaffolds. Gyroid topology was selected due to its interconnected porosity and superior, isotropic mechanical properties compared to typical rectilinear lattice structures. Our 3D printed scaffolds were mechanically tested in compression and examined to determine the relationship between porosity, ultimate compressive strength, and fracture behavior. Compressive strength increased with decreasing porosity. Ultimate compressive strengths of the 60% and 70% porous gyroids are comparable to that of human cancellous bone, and higher than previously reported for rectilinear scaffolds of the same material. Our gyroid scaffolds exhibited ultimate compressive strength increases between 1.5 and 6.5 times greater than expected, based on volume of material, as porosity decreased. The Weibull moduli, a measure of failure predictability, were predictive of failure mode and found to be in the accepted range for engineering ceramics. The gyroid scaffolds were also found to be self-reinforcing such that initial failures due to minor manufacturing inconsistencies did not appear to be the primary cause of premature failure of the scaffold. The porous gyroids exhibited scaffold failure characteristics that varied with porosity, ranging from monolithic failure to layer-by-layer failure, and demonstrated self-reinforcement in each porosity tested.

ACKNOWLEDGEMENTS

I would like to thank several people who have aided and guided me throughout this process and journey. I would like to first thank Dr. David Prawel for taking me on as a student and for believing in me from the start. You have reiterated to me that you wouldn't have chosen me if you didn't think I could accomplish all of this; thank you for having that faith and trust in me, even when I didn't necessarily believe it myself. I would like to thank Dr. Susan James for being an additional source of encouragement and reinforcement, for being a voice of calm and reassurance when you felt that I needed it. I would like to thank my colleagues at BRELAB here at CSU: the work presented here by no means came out of a vacuum. I am but one in a series of grad students: Katherine Lopez Ambrosio previously developed the material that I got to spend two years playing with and Adam Schneiderhan will (hopefully) be able to use my results while building his own work. I have had the pleasure of working with several amazing undergrads at BRELAB; Nathan Waanders, Emily Hoffmann, Connor Witt, Cara Leone, Maddie Shafer, Erik Christoffersen, and Genesis Marrero have all impacted this work one way or another, whether over the course of the full two years or in the last few months as the future direction of this work was laid out. I would like to thank SAMD and my peers here at CSU for creating an unbelievably welcoming and supportive environment and camaraderie that I know will be held near and dear to me for life. I would like to thank my parents for helping build me up into the adult I became (and am still working on!), for instilling the drive towards learning, and for helping set me on a life path that I truly enjoy.

Most importantly, I would like to thank my wife, Katie. Without your love, your support, and your unwavering commitment, I doubt that I ever would have had the courage to pursue this

degree, let alone finish it. You have been my rock and my support; everything you've done to help me, from intently listening to me ramble about test methods or 3D printing or porosity measurements, giving feedback on presentations styles, to simply bringing me a cup of tea while I write at my desk has contributed massively towards completion of this work. I know I have been stressed over all this, spending long days and nights away mentally, but I know it'll be worth it. I love you.

Chris Hadfield, in his book "An Astronaut's Guide to Life on Earth: What Going to Space Taught Me About Ingenuity, Determination, and Being Prepared for Anything", wrote "I've realized that in any new situation, whether it involves an elevator or a rocket ship, you will almost certainly be viewed in one of three ways. As a minus one: actively harmful, someone who creates problems. Or as a zero: your impact is neutral and doesn't tip the balance one way or the other. Or you'll be seen as a plus one: someone who actively adds value." When I first started researching graduate programs, all while grinding away at a desk as a cog in a machine, I was unsure if I could even reach a zero in grad school. I kept going anyway. After initial struggles adjusting back to academia, I settled in and felt secure in my work for the first time in a long time. After the COVID pandemic started and everything switched to working from home, I struggled to adjust. I kept going anyway. When time was running short and I needed to delay graduation, I kept going anyway. While reflecting on the last few years, I realized that a minus one would have simply quit a while ago and that a zero would never have started in the first place. Pushing through, continuing, and ultimately finishing means I've been a one all along. Finally recognizing this fact, quite honestly, is a pretty good feeling.

TABLE OF CONTENTS

ABSTRACT.....	ii
ACKNOWLEDGEMENTS.....	iv
TABLE OF CONTENTS.....	vi
LIST OF FIGURES	viii
OVERVIEW	1
CONTRIBUTIONS	6
ARTICLE MANUSCRIPT.....	8
SUMMARY	8
INTRODUCTION	9
MATERIALS AND METHODS.....	15
Scaffold Materials & Processing	15
Rheological behavior, viscosity and homogeneity	16
Scaffold Design.....	17
3D Printing.....	18
Sintering.....	18
Scaffold Dimensions & Shrinkage.....	18
Micro-computed tomography, Scaffold Porosity & Pore Size	19
Thermogravimetric Analysis	19
Cytotoxicity Analysis.....	20
Compression Testing	22
Scanning Electron Microscopy	24
Statistical Analysis.....	24
RESULTS	25
Rheological behavior, viscosity and homogeneity	25
Scaffold Dimensions & Shrinkage.....	27
Micro-CT: Total Volume, Filled Volume, Scaffold Porosity & Pore Size	27
TGA/EDS.....	28
Cytotoxicity.....	31
Compression Testing	31
Failure Modes	34

DISCUSSION.....	37
Rheology.....	37
Comparing As-Designed and As-Built Scaffolds.....	37
TGA/EDS.....	39
Cytotoxicity.....	40
Scaffold Consistency	40
Compressive Strength/ Construct Modulus	43
Failure Modes	48
CONCLUSIONS.....	52
REFERENCES	54
APPENDIX.....	60
Appendix A: 41% Vol hydroxyapatite slurry mixing protocol	61
Appendix B: Creating gyroid files for 3D printing.....	63
Appendix C: Compression testing of porous ceramic scaffolds.....	65

LIST OF FIGURES

Figure 1: A printed 80% porous gyroid. The x-y plane is parallel with the scaffold build surface, i.e. the z-direction is the “height” axis. In normal testing, load is applied parallel with the z-axis, perpendicular to the x-y plane. In transverse testing, load is applied parallel with either the x-axis or y-axis, into the y-z or x-planes, respectively.	22
Figure 2: Shear rate vs Apparent Viscosity of the HAp slurry.	25
Figure 3: Shear rate vs Apparent Viscosity at different storage times.	26
Figure 4: TGA results for green scaffold material.	29
Figure 5: SEM of green body surface. EDS layered images of oxygen, phosphorous, calcium, and carbon are shown in the red, blue, green, and purple maps, respectively.	30
Figure 6: SEM of green body. EDS line scan paths shown in red. Line data results are shown on the right.	30
Figure 7: Ultimate compressive strength varies by porosity and direction. The dotted line denotes the lower limit of human cancellous bone strength. * = significantly different ($p > 0.05$).	32
Figure 8: Failure probability for each scaffold set as determined via Weibull distribution. Steeper curves indicate more consistent failure stresses.	33
Figure 9: Compressive modulus remains similar for the 60% and 70% porous gyroids but is significantly lower for 80% porous scaffolds. * = significantly different ($p > 0.05$).	34
Figure 10: Fracture surface of a 70N scaffold. Location 1 shows a surface crack penetrating into the scaffold. Locations 2 and 3 show the crack progressing along the internal interface between roads.	35
Figure 11: Failure path of an 80T sample from recorded video footage. A) The scaffold before loading. The circles indicate preexisting surface cracks. B) Initial failure of the scaffold. The preexisting cracks have propagated through the roads and are extending through the structure. C) Final failure of the scaffold. Cracks and local failures are present throughout the structure.	36
Figure 12: Micro-CT imaging of a 60% porous scaffold. Green regions indicate nominal material thickness, orange regions indicate greater material thickness.	38
Figure 13: Fracture surface of a 60N scaffold. The arrows point towards the concentric ring present along the roads. The ring is delaminating in the upper-right corner of the exposed surface.	41
Figure 14: Fracture surface of an 80N scaffold. Interior cracks extend from the concentric ring towards the core of the road.	42
Figure 15: Representative moduli. Red = as measured. Black vertical line = manual measurement. A) Measurements align closely. B) Early failure - standard modulus < effective modulus. C) Effective modulus < standard modulus. D) Self-reinforcement after initial failure – second phase of the curve has a modulus similar to the first phase.	47
Figure 16: A section of an 80N showing a failed section reinforced against neighboring material.	49

Figure 17: Failure surface of a 70N scaffold. Note that the surface cracks penetrate each rod interface along the side of the scaffold strut that experiences tension in this scenario, whereas the surface cracks along the compression side appear less organized. 50

Figure 18: SEM of a sintered scaffold. A) shows the fully densified surface grains. B) shows the micropores between HAp grains. The dense surface grains extend approximately 0.5-2 μm into the rod, as shown with the narrower arrow region. The concentric ring is marked by the larger span of arrows. 52

OVERVIEW

Research into synthetic bone grafts has been an active field over the past several decades. However, published literature tends to focus on individual facets of synthetic graft design rather than exploring how these facets effect other scaffold properties. It is common to find literature that discusses, for example, designs with different porosities without also discussing how the porosities affect mechanical response. Similarly, published articles will discuss compressive strengths but only when tested in one direction, neglecting discussion of potential anisotropy in the scaffold. In this work, we theorized that manufacturing a well-known material, hydroxyapatite (HAp), into a more efficient structure would yield a scaffold that would be mechanically sufficient for a cancellous bone graft despite being made from a material that had been regarded as inadequate for such use. Significant effort was made to include as many facets of scaffold design and characterization as were feasible. The development and characterization of these scaffolds resulted in a manuscript intended for future submission for publication in the Journal of Biomaterials Applications. An overview of this project is presented first, followed by an expanded version of the manuscript containing additional discussion, results, and figures. Statements made in the overview are presented and intended as generalities: specific claims, supporting information, and citations are presented in the manuscript.

Critically sized bone defects affect millions of people a year and require surgical procedures such as external fixation. This results in billions of health care costs for treatment and therapy, along with the risk of continual procedures and life-long issues. Natural bone auto/allo-grafts are preferential, but the risk of failure remains high; additionally, the shortage of material limits their availability. Synthetic metallic implants are readily available but significantly reduce the body's

ability to remove waste byproducts from the healing process. Many ceramic materials exist that may serve as synthetic grafts, but biocompatible materials are often mechanically inadequate. Hydroxyapatite is one such material. The biocompatible nature of HAp has been long known, however the mechanical properties of HAp in traditional scaffold designs are inadequate. Synthetic scaffolds with advanced topologies such as gyroids, a type of triply periodic minimal structure, can potentially mitigate these mechanical property limitations due to their inherent structural advantages. However, manufacturing of these structures is difficult. New additive manufacturing methods are beginning to show promise in overcoming the challenges associated with this new generation of scaffold design.

In our work, we present a method of robocasting combined with photopolymerization, which we refer to as photocasting. This method is capable of producing complex scaffolds such as gyroids without requiring support material. HAp particles are suspended in a colloid consisting of a monomer, a photoinitiator, and a dispersant, using a method developed by my predecessor, Katherine Lopez-Ambrosio. The materials are mixed via ball-milling to create a homogenous slurry. The rheology and homogeneity of the slurry were evaluated by Lopez-Ambrosio to ensure printability. Gyroids with 60%, 70%, and 80% relative porosity were designed using Autodesk Fusion 360 and sliced via Cura. The resultant GCode was used with a Hyrel Hydra, equipped with an EMOXT print head, to print the HAp slurry. An array of 405nm wavelength LEDs was used to cure the slurry as it was being printed, resulting in near-net-shape scaffolds. The scaffolds were then sintered at 1200°C to debind (via vaporization) the organic components and densify the HAp. The resultant sintered scaffolds then consist of only HAp.

The scaffolds shrink during sintering and so the dimensions were recorded to appropriately scale future designs. Micro-CT was used to determine porosity and to measure internal connectivity of

the scaffold structure. Thermogravimetric analysis (TGA) was used to confirm the organic component pyrolysis. Energy dispersive X-ray spectrometry (EDS) was used to confirm homogeneity in printed green (non-sintered) structures. The biocompatibility of the scaffold material was also evaluated using mesenchymal stromal cells. The cells were designed to express luciferase, which is bioluminescent and visible using *in vivo* imaging techniques. Cylindrical rectilinear scaffolds, both green and sintered, were used as the base substrate for cytotoxicity evaluation led by Lopez-Ambrosio. Cell proliferation was tracked through 10 days and cell morphology was evaluated during the study.

Lopez-Ambrosio found that viscosity decreased as shear rate increased in a phenomenon known as shear-thinning. She also confirmed that viscosity is stable as storage time increases up to at least 20 days. The green scaffold dimensions were within 0.6%-1.3% of designed dimensions. The sintered scaffolds shrunk 20.48%-21.33% during sintering. Micro-CT shows that the internal pores of the scaffolds are fully interconnected though the total relative porosity differs by 3.51%-10.40% from design. TGA results of green material indicate the organic components vaporize above 250°C. TGA results of sintered material indicate that no further vaporization occurred, showing that the sintering process removed the organic materials. The cytotoxicity study results show that sintered scaffolds are not cytotoxic, whereas the green scaffolds are cytotoxic.

The mechanical properties of the gyroid scaffolds were evaluated using compression testing. Scaffolds were tested both normal and transverse to the build direction in order to evaluate scaffold isotropy. The samples were tested with a 1 kN load cell with a crosshead displacement rate of 0.1 mm/min. Video footage of the tests was recorded to analyze global failure modes. The stress-strain curves were evaluated to determine mechanical properties and a novel construct modulus was developed to evaluate effective structural stiffness in parallel to the standard

method of measuring compressive stiffness. Scanning electron microscopy (SEM) was used to view both the scaffold surfaces as well as the fracture surfaces of tested scaffolds.

Compression testing of our scaffolds show that ultimate compressive strength decreases from a peak strength of 4.29 MPa to 0.36 MPa as porosity increases. The scaffolds tested normal to the build direction are significantly stronger than those tested transversely to the build direction. The Weibull modulus, a method of predicting failure and variance for materials susceptible to flaw-dependent failure, of the scaffolds was predictive of failure mode and found to be between 3-5 suggesting that these scaffolds could be used in engineered designs. The compressive moduli were found to be consistent for all directions at 60% and 70% porosity, between 73 MPa and 83 MPa, but decrease significantly to 45 MPa – 46 MPa at 80% porosity. Analysis of the test footage show that the scaffolds exhibit either monolithic failure or layer-by-layer failure and that the global failure mode is greatly affected by the porosity of the structure. The tested direction affects the local failures in the material. In all cases, failure initiates at surface cracks found throughout the scaffolds.

The rheology study (done by Lopez-Ambrosio) affirms the shear-thinning behavior of the material. Shear-thinning allows the slurry to be more easily printed but potentially contributes to inconsistencies in printing. Scaffold dimensions (as-printed) deviate from as-designed in specific areas; these inconsistencies result from inconsistent material deposition, theorized to be due to the effects of the shear-thinning in the nozzle during printing. Shrinkage during sintering was isotropic and therefore able to be used as a design parameter. A combination of factors leads to cracks throughout the scaffolds. The cure depth is theorized to be shallow due to the opacity of the material, though we were unable to pursue this further, and is hypothesized to affect the thermal expansion properties of the material. The changes in thermal expansion led to internal

thermal stresses during sintering and the excess energy is released via crack formation at the junctions between printed roads and in internal concentric cracks.

The increased ultimate compressive strength of the scaffolds when tested in the normal direction is hypothesized to be a result of additional road overlap during printing. This increased road boundary increases the effective area that experiences stress, thus increasing the strength of the scaffold. Conversely, the transversely tested scaffolds are theorized to experience higher rates of local bending, which has a tensile component, within the printed struts, thus leading to earlier failure. The Weibull modulus was found to be within the range of engineering ceramics for five of the six tested sets, thus indicating that these scaffolds are sufficiently predictable to be used as engineered structures. The failure probability graphs, derived from the Weibull modulus, correlate with the failure modes exhibited by each sample set. The consistency in compressive modulus for 60% and 70% porous scaffolds, compared to the significantly lower value for 80% porous scaffolds, imply that a critical porosity exists above 70%, resulting in a sharp decrease in the compressive modulus. The compressive construct modulus, used to evaluate effective stiffness of the overall structure, consistently accounted for failure behavior within the scaffolds and proved to be a valuable method for predicting scaffold behavior. Comparisons between our structures and other structures are difficult to determine due to the range in materials, methods, and structures used. In general, our scaffolds were found to have higher ultimate compressive strengths and high compressive modulus values than other robocast HAp scaffolds with similar porosity.

Initial failure sites were found to correspond to surface crack locations. As the scaffolds begin to fail under loading, sections of the scaffolds that break earlier tend to self-reinforce against neighboring material, a phenomenon seen in architectural arches. This self-reinforcement was

more common in normally tested scaffolds than in transversely tested scaffolds. The surface and internal cracks were determined to be the most significant factor to earlier failure of the structures. Further study is required to determine if the scaffolds can be further strengthened by altering the sintering profile. Reduction of crack sites is hypothesized to be achievable by reducing the ramp rate, thus allowing more time for organic component vaporization and HAp grain densification. The longer sintering time yields larger grain sizes, which would weaken the structures, but increases the density of the material more significantly, leading to a stronger structure.

Both normal and transverse 60% scaffolds, as well as the transverse 70% porous scaffolds, were found to have ultimate compressive strengths sufficient to potentially serve as cancellous bone grafts. The self-reinforcing nature of the material indicates that an implanted scaffold may survive initial loading and potential initial damage, thus allowing the body to continue to build new bone upon the scaffold and continue to integrate the graft in the normal healing process. Additional research into the sintering profile is recommended, as is studying the effects of cure depth on material densification and scaffold mechanical properties.

CONTRIBUTIONS

Several individuals contributed to this work and have been identified as contributing authors as a result. Katherine Lopez-Ambrosio created the slurry used through this work and led the studies of rheology, homogeneity, and cytotoxicity. Laura Chubb performed the cytotoxicity work. Nathan Waanders contributed significant time throughout the entirety of this work to fine-tuning the printing process and developing the printing procedure. Emily Hoffmann performed the TGA work, fine-tuned our sintering profile, and led preliminary work into porosity measurement

methods. Connor Witt assisted with developing the gyroid digital model generation methods. Susan James ensured that the direction and discussion regarding mechanical properties were performed accurately and served as a reference for understanding the tendencies inherent to ceramic structures. David Prawel, the principal investigator for this project, established the basis for the initial investigation, guided the overall direction of the project, and provided significant knowledge and insight regarding background literature and understanding of how this work fits in to the broader picture.

SUMMARY

Hydroxyapatite is commonly used in tissue engineered scaffolds for bone regeneration due to its excellent bioactivity and slow degradation rate in the human body. A method of layer-wise, photopolymerized viscous extrusion, a type of additive manufacturing, was used to fabricate hydroxyapatite gyroid scaffolds with 60%, 70% and 80% porosities. Our study is the first to use this method to produce and evaluate calcium-phosphate-based scaffolds. Gyroid topology was selected due to its inter-connected porosity and superior, isotropic mechanical properties compared to typical rectilinear lattice structures. Our 3D printed scaffolds were mechanically tested in compression and examined to determine the relationship between porosity, ultimate compressive strength, and fracture behavior. Compressive strength increased with decreasing porosity. Ultimate compressive strengths of the 60% and 70% porous gyroids are comparable to that of human cancellous bone, and higher than previously reported for rectilinear scaffolds of

¹ Compressive Properties and Failure Behavior of Photocast Hydroxyapatite Gyroid Scaffolds Vary with Porosity

Authors: Nelson Isaacson¹, Katherine V. Lopez-Ambrosio¹, Laura Chubb, Nathan Waanders, Emily Hoffmann, Connor Witt, Susan P. James^{1,2,3}, David A. Prawl^{1,2,3}

¹: School of Advanced Materials Discovery, Colorado State University

²: Department of Mechanical Engineering, Colorado State University

³: School of Biomedical Engineering, Colorado State University

Corresponding Author: David Prawl, david.prawl@colostate.edu

Permanent Address: Engineering, 1374 Campus Delivery, Fort Collins, CO 80523

Declaration of interests: The authors declare that they have no known competing financial interests or personal relationships that could have appeared to influence the work reported in this paper.

the same material. Our gyroid scaffolds exhibited ultimate compressive strength increases between 1.5 and 6.5 times greater than expected, based on volume of material, as porosity is decreased. The Weibull modulus, a measure of failure predictability, was found to be in the accepted range for engineering ceramics. The gyroid scaffolds were also found to be self-reinforcing such that initial failures due to minor manufacturing inconsistencies did not appear to be the primary cause of early failure of the scaffold. The porous gyroids exhibited scaffold failure characteristics that varied with porosity, ranging from monolithic failure to layer-by-layer failure, and demonstrated self-reinforcement in each porosity tested.

Keywords: Additive Manufacturing, Gyroid, Scaffold, Robocasting, Mechanical Testing, Porosity

INTRODUCTION

Poor healing of critically sized bone defects affects 1.5 million Americans per year and results in more than \$1 billion in treatment and therapy cost[1]. Treatment options remain limited and often lead to reoperations, clinical complications, poor functional outcomes, and limb loss, making this one of the biggest challenges in orthopedic medicine, resulting in significant personal and economic cost[2]. Healing strategies using autografts, allografts and xenografts are limited by shortage of available tissue and failure to heal[3], with complication rates of 50% from delayed or non-union, 30% from allograft fracture, and 15% from infection[4]. Decades of research has been dedicated to solving this problem using a wide variety of bone regeneration techniques. Tissue engineered solutions have emerged that deploy biodegradable, osteoconductive scaffolds to provide structural support and osteoinductive stimulus, with suitable porosity to enable nutrient and waste exchange and angiogenesis[5]–[7]. Promising calcium phosphate biomaterials like hydroxyapatite (HAp) and β -tricalcium phosphate are

widely studied for bone regeneration scaffolds due to their excellent bioactivity (osteinductivity, osteoconductivity and osseointegration), mineral composition and tunable degradation rates[8], [9].

A synthetic scaffold must meet several key requirements to successfully support new bone growth and development. The scaffold must be non-cytotoxic, promote bioactivity, allow adequate gas, nutrient and waste exchange, and degrade at an appropriate rate to enable new bone growth[6], [7]. Cytotoxicity and bioactivity are dependent on the scaffold material itself, while degradation rate is affected by both the material and the scaffold structure [10], [11]. To facilitate the fluid exchange, the scaffold must be adequately porous. Scaffold porosity can refer to either micro porosity or macro porosity. Micro porosity is determined via density of the material and requires measurements of the spacing between the grains within the material itself. Macro, or “relative”, porosity is measured using the designed pore sizes in the structure. Relative porosity is generally what is referred to when discussing artificial scaffolds [12]. Mechanically, suitable scaffolds must be able to support loads imposed upon them during the healing process while matching the mechanical properties of the surrounding host bone and providing adequate porosity and permeability to support bone regeneration[13]. Despite excellent bioactivity and bone regeneration properties, success of calcium phosphate scaffolds is hampered by inadequate structural properties required for significant load-bearing[12]. To date the preponderance of research has targeted this challenge by developing improvements to the bulk biomaterial. Most of this work has been rewarded with relatively small improvements in mechanical properties that unfortunately still fall far short of the required mechanical strength for significant load bearing. An alternative approach to engineering the bulk biomaterials is to develop more complex structures and topologies that will improve structural properties. Enhancing the structure without

altering the biomaterial enables the scaffold to maintain its excellent bioactivity with higher porosities in higher loads.

Advanced scaffold topologies such as a type of triply periodic minimal surface (TPMS) structure called gyroids[14]–[16] are yielding scaffolds that are stiffer and stronger than traditional rectilinear scaffold topologies[17]–[20]. Gyroids are ideal candidates for scaffold designs due to their relatively high mechanical energy absorption and robustness, interconnected internal porous structure, scalable unit cell topology, and smooth internal surfaces with relatively high surface area per volume[17], [18], [21]. High mechanical energy absorption and robustness enables gyroid structures to bear relatively higher loads than typical rectilinear scaffolds of the same dimensions[16]. Continuous interconnected pores enable designed permeability and perfusion throughout the structure, which enables good nutrient and waste diffusion[22], [23]. Scalable unit cell topology enables engineering of structures to meet specific requirements, such as porosity, permeability and functional grading[21], [24], [25]. Smooth internal surfaces with relatively large curvature avoid the abundant stress concentration sites that plague rectilinear topologies[16]. Since they lack abrupt changes in direction, they are less likely to provide internal resistance to fluid flow due to head loss. Moreover, marrow stromal cells grow faster on larger curvatures such as in gyroid topologies[16]. In a recent study, gyroid models were found to have more consistent cell adhesion and were judged as the better choice for most TE applications among TPMS structures studied[26]. Production of complex scaffold topologies require advanced fabrication techniques.

Additive Manufacturing, also known as 3D printing (3DP), is a popular method of fabricating complex scaffolds with precise internal architectures. Patient-specific scaffolds can be created directly from CT scans, ensuring the scaffolds precisely fit a defect site, which improves

outcomes[27]. Well-fitting implants more broadly transfer loads through the limb and devices, reducing the risk of localized stress-induced failure. 3D printing enables creation of complex scaffold shapes that accommodate interrelated parameters such as porosity, pore size and permeability, all of which play a role in the success of a scaffold[14], [17], [23]. Numerous additive processes are employed in development of the huge variety of scaffold materials, shapes and applications under consideration. The more popular approaches for ceramic bone regeneration scaffolds are binder jetting, powder bed fusion (PBF, sintering or direct melting) and viscous extrusion[28]. Recent excellent reviews discuss the advantages and disadvantages of various 3DP processes in a wide array of materials, topologies and applications[12], [18], [29], [30].

Binder jetting and PBF create scaffolds from beds of powder. In PBF, an energy source (laser or electron beam) is directed at a bed of powder. The energy binds the powder particles by sintering (direct or indirect) or melting, depending on the amount of energy applied and the material. Depending on the density desired, a third infiltrant material may be applied to densify sintered objects. Binder jetting also involves a bed of powder but instead of applying an energy source, one or more binder materials is jetted onto the powder bed using relatively simple ink-jetting technology. Like PBF objects, binder jetted parts also often require a secondary densification process depending on density desired and material. Binder jetting is a relatively low cost and very flexible method of making scaffolds using a wide variety of binders and materials[31]. Material jetting also jets material to create parts. But contrary to binder jetting which jets a binder onto a material that becomes the final object, material jetting jets a photopolymeric material that comprises the final object. The material is jetted in successive, thin layers onto a platform that lowers as the subsequent layers are jetted, along with a sacrificial material to

support the object while it cures. Materials can be loaded with nanoparticles of many different types of rigid material like ceramics and metals. Photopolymerization uses light to initiate a polymerization reaction that cures a liquid resin precisely where the light contacts the resin[32]. For scaffold fabrication, this is often accomplished on the surface of a vat of resin, in which a very thin layer of resin is cured as a laser quickly passes over the vat, then a very thin layer of resin is spread over the surface and the laser cures the next layer, and so on to create the object. Viscous extrusion is a popular, low-cost process that prints a broad variety of highly viscous slurries which harden by evaporation or active removal (e.g. by pyrolysis) of the liquid component[33]–[36]. A type of viscous extrusion called robocasting is a very low cost and highly flexible method of fabricating scaffolds.

Excellent reviews [12], [27], [37] provide a comprehensive overview of the advantages and disadvantages of the various additive processes for using ceramic biomaterials in tissue engineering. Photopolymerization and viscous extrusion processes depend on material flow to accurately print thin layers in processes referred to as colloidal ceramic processing[30]. In polymerization, ceramic particles can be suspended in the photopolymeric resin. A high volume-fraction of ceramic material is necessary to achieve low micro porosity (and thus higher strength) in the ceramic structure following the removal of the binding component. This is difficult to achieve because suspended ceramic particles greatly increase the colloidal slurry viscosity [38], and thus it is challenging to create objects with both high volume fraction ceramic as well as high precision. This makes these highly viscous slurries, as required for ceramic scaffolds, very difficult to 3D print using photopolymerization[12].

In robocasting, complex ceramic structures are fabricated by extruding highly viscous slurries composed of ceramic particles suspended in volatile solvents or polymers. As in

photopolymerization, it is challenging to use high volume fractions of ceramic slurries while maintaining low enough viscosity to 3D print complex shapes in high precision[30]. Scaffolds made using robocasting must be sintered to densify the ceramic object and remove the organic and polymeric components. In these slurries, viscosity can be adjusted by using a dispersant to keep the particles in suspension, enabling a higher solid loading, which decreases micro porosity in the sintered structure. Robocasting is simple, low cost and very flexible [39], enabling creation of a broad variety of ceramic structures using a very wide choice of materials.

Unfortunately, it is difficult using robocasting to fabricate scaffolds with both complex topology and mechanical integrity. Fabrication of mechanically superior structures like gyroids require the ability to print slurries with high solid content and allow time for the soft extruded material to harden. Therefore, overhangs must be supported by additional material that must later be removed, which limits topological complexity. This limitation has led to a new approach that combines multiple AM techniques. By combining layer-wise photopolymerization with robocasting, printed layers can be cured as they are printed, eliminating the need for support material and enabling fabrication of highly complex, high precision structures. We refer to this method as “Photocasting”. Faes et. al.[40] was the first to use this approach to fabricate featureless slabs of yttrium-stabilized Zirconia. Asif et al.[41] and Farahani et al.[42] combined viscous extrusion with photopolymerization to produce fairly simple self-supporting structures consisting of a photopolymeric resin containing fumed silica particles to adjust slurry viscosity. Our study is the first to use this method to produce and evaluate calcium-phosphate-based scaffolds involving complex, overhanging internal structure.

Photocasting of complex gyroid structures enable engineering of specific relative porosities, permeabilities, pore sizes, pore orientation, interconnectivity, and other parameters throughout

the scaffold, considered essential for successful scaffolds. Photocast scaffolds can be engineered to provide specific fluid flow while printing advanced structural topologies to maximize mechanical properties, even functionally grading topology and associated properties within a scaffold. Several studies have investigated how these internal architectures affect the bioactivity of a scaffold [43]–[46].

In this study we photocast gyroid scaffolds with designed interconnected pores using a photopolymerizable HAp slurry. 3D printed green structures were sintered to remove polymeric content and increase bulk density. Using photocasting we were able to fabricate complex structures with very high precision compared to other 3D printing methods. Our scaffolds demonstrate ultimate compressive strengths in the range of human cancellous bone, and higher than previously reported for rectilinear scaffolds of the same material. To this end, this paper evaluates compressive strength and fracture behavior of 3D printed HAp gyroid scaffolds of various porosities and compares to literature of rectilinear scaffolds of similar materials.

MATERIALS AND METHODS

Scaffold Materials & Processing

Gyroid scaffolds were fabricated from a HAp-loaded photopolymeric resin that was developed in prior work [47] then 3D printed and finally sintered. A light-sensitive liquid monomer was used to suspend HAp particles, enabling 3D printing by viscous extrusion and layer-wise photo-curing (photocasting). The liquid monomers assured dispersion of HAp in the resin colloidal phase, while the crosslinked network of monomers formed the immobilized HAp particles into the as-printed shape.

The colloid's continuous phase consisted of 99% pure ethylene glycol dimethacrylate (EDGMA, Scientific Polymer Products, Inc., Ontario, NY, USA) as the monomer and diphenyl (2,4,6, trimethyl benzoyl) phosphine oxide (TPO, TCI America, Portland, OR, USA) as the photoinitiator. These constituted the light sensitive system. The colloid's dispersed ceramic phase consisted of needle-like HAp particles (Macron Fine Chemicals, Avantor, Radnor, PA, USA), 85nm long (nominally) with 67 m²/g specific surface area. A commercial anionic dispersant, Solplus D540 (Lubrizol Advanced Materials Inc., Wickliffe, OH, USA) was added to reduce viscosity by dispersing the HAp particles in the monomer.

EGDMA, TPO, and D540 were mixed with agate milling media in Teflon[®] jars on a planetary ball mill (Across International, Davie, FL, USA) at 120 rpm for 15min. Jars were sealed to avoid vaporization of EGDMA. HAp particles were gradually added to the solution in three different increments, resulting in a homogeneous slurry. Following the ball-milling process, the agate media was removed, and the mixture was hand-stirred for an additional 5 minutes. The resulting slurry was then either stored airtight, wrapped with aluminum foil to avoid exposure to light or directly transferred to the 3D printer. This process produced 41 vol% HAp slurries.

Rheological behavior, viscosity and homogeneity

Rheological behavior and viscosity of HAp slurries were evaluated at 25°C with a parallel plate rheometer (Ares, TA Instruments, New Castle, DE, USA). Approximately 1 ml of HAp slurry was placed between the two 2.5cm diameter parallel plates, which were brought together until a gap of 1.1 mm was reached, at which time the sample was allowed to relax for five minutes. Apparent viscosity was measured at 0.1 s⁻¹, 1 s⁻¹, 10 s⁻¹, 100 s⁻¹ shear rates.

The rheological behavior of the HAp slurries was also evaluated as a function of storage time to identify any possible changes in viscosity due to storage conditions (light-sensitive material). Apparent viscosity as a function of shear rate was measured over a period of 20 days.

The homogeneity of the slurry was confirmed by evaluating the distribution of the elemental composition of carbon, oxygen, calcium, and phosphorus in the “green” (unsintered) scaffolds with Energy Dispersive X-Ray Spectroscopy (EDS) [47].

Scaffold Design

Gyroid scaffold models for compression testing (10 mm x 10 mm x 10 mm cubes) were designed using CAD (Autodesk Fusion 360, Sausalito, CA, USA). The model was exported in STL format and then sliced using Cura (<https://ultimaker.com/software/ultimaker-cura>). Length is correlated to the x axis, width is correlated to the y axis, and height is correlated to the z axis when imported into Cura. During the slicing process, a gyroid infill pattern was selected to create the interconnected pore structure. Perimeter, surface, and base shell layers were set to zero to isolate the gyroid infill, which was set to result in desired relative porosities of 60%, 70%, and 80%. Line width was set to 413 μm , layer height was 200 μm , and print speed was 2 mm/s to ensure consistent layer width. This results in several distinct roads per layer as seen in Figure 1. Fully dense (100% infill) rectangular prisms (8 mm long (x) x 6 mm wide (y) x 6 mm tall (z)) were also fabricated for material characterizations such as thermogravimetric analysis and as controls for shrinkage calculations. The resultant G-code was exported as a .txt file and modified to be used on the Hyrel printer.

3D Printing

Sixteen scaffolds of each porosity, along with control slabs, were printed using a Hyrel Hydra (Hyrel 3D, Norcross GA, USA) using an EMOXT reservoir print head (Hyrel 3D) equipped with a 22-gauge syringe tip. This print head is also equipped with an array of LED lights (405nm wavelength, light power density ranging from 0.7 mW/cm² to 1.3 mW/cm²) mounted near the base of the print head to photo-cure each layer as it is printed. The photopolymerization reaction was initiated by continuous exposure of the deposited roads to the light source, causing layer-wise polymerization and hardening of the continuous phase. “Green” scaffolds are printed onto a borate glass build platform, which is covered with painter’s tape to enhance bed adhesion and to reduce clogging of the print nozzle caused by UV light reflecting upward into the nozzle. When 3D printing finished, the HAp/PEGDMA green scaffolds stored in the dark at room temperature until they were sintered.

Sintering

The HAp/PEGDMA green scaffolds were sintered to remove organic content as well as to densify the hydroxyapatite within the scaffold struts. Green scaffolds were placed in a muffle furnace (Barnstead/Thermolyne 47900, Ramsey, MN, USA), heated at a ramp rate of 5°C/min up to 1200°C and held for 3 hours. The furnace was allowed to cool to ambient temperature and the scaffolds were removed and kept dry in a desiccator under vacuum.

Scaffold Dimensions & Shrinkage

After sintering, scaffold dimensions decreased (shrinkage) due to the coalescence of HAp particles and the pyrolysis of PEGDMA and other organic constituents. Samples were measured in three axes using calipers before and after sintering. Actual dimensions after shrinkage were

used to appropriately scale initial CAD designs to achieve desired net-shape dimensions and pore sizes. Printed rod diameters were measured directly from SEM images using ImageJ (National Institutes of Health, Bethesda, MD, USA).

Micro-computed tomography, Scaffold Porosity & Pore Size

Micro-computed tomographic (micro-CT) imaging was performed using a Scanco 80 (Scanco Medical AG, Bruttisellen, Switzerland) to measure scaffold relative porosity and pore size. The micro-CT device was pre-loaded with parameters designed to scan bone and porous bone-like materials. Three key measurements were recorded from the scans: Total Volume (TV), Filled Volume (FV), and Mean Spacing (MS). TV is defined as the nominal volume occupied by the scaffold, FV is defined as the volume of material within the TV, and MS is defined as the average spacing between material in the scaffold. MS is used as the measure of average pore size. TV and FV were used to determine relative porosity (ϕ) using the following equation:

$$\phi\% = 1 - \frac{TV}{FV} * 100\%$$

Thermogravimetric Analysis

Thermogravimetric Analysis (TGA) was used to confirm the range of temperatures at which the organic components are vaporized, as well as to confirm complete removal of the organic components after a scaffold was fully sintered. Two separate samples were tested: a sample of green scaffold, obtained before sintering the scaffold, and a sample of a sintered HAp scaffold sample. Both were ground, separately, to a fine powder. A TGA pan was cleaned with ethanol and burned clean with a Bunsen burner flame. The pan was tared on a Thermogravimetric Analyzer (TA Instruments Q500, New Castle, DE, USA) before 12.4mg of the powder was

added to the pan. Data was collected as the analyzer heated the sample from 25°C to 500°C at a rate of 5°C/min. After heating, the temperature was ramped quickly (50°C/min) back to 25°C. Weight percent and weight change percent were recorded.

Cytotoxicity Analysis

Mesenchymal stromal cells were harvested from the abdominal adipose of mature luciferase expressing Wistar rats using a well-established method [48]. These adipose-derived MSCs (AD-MSCs) ubiquitously expressing luciferase were cultured in Dulbecco's Modification of Eagle's Medium (DMEM; Corning, Manassas, VA, USA) supplemented with 15% fetal bovine serum (FBS; Atlas Biologicals, Fort Collins, CO, USA), MEM vitamins, non-essential amino acids, and antibiotic-antimycotic in a 5% CO₂ and 95% air atmosphere at 37° C.

Bioluminescent imaging (In Vivo Imaging System (IVIS) Spectrum, Perkin Elmer, Waltham, MA, USA) was used to confirm AD-MSC cells expressed the luciferase gene, using an established protocol [49]. Briefly, a well containing 1×10^5 cells was exposed for 1 min and high sensitivity binning was used to enhance quantification of the cells. The minimum intensity was set at 10% of maximum and a contour region of interest (ROI) plot with default parameters (ROI edge value of 5%) was chosen to increase objectivity of quantification. Total flux of the ROI was recorded as photons/sec for each sample. Images we analyzed using Living Image Software (Living Image 4.2; Perkin Elmer).

Quantification of luciferase intensity was performed by creating a standard curve. AD-MSCs were serially diluting *in vitro*, and bioluminescence was quantified using the IVIS system. Bioluminescent intensity correlated linearly with increased cell number as defined by a standard curve ($r^2 = 0.9865$, $P < 0.05$).

Cylindrical scaffolds, 8 mm diameter x 3 mm height with rectilinear infill, were 3D printed using the method described in this paper. Six each of green (G) and sintered scaffolds (S) were printed (N=6 for both groups). All scaffolds were sanitized by soaking for 1 hour in 99% ethanol.

All scaffolds were then placed in 24-well tissue culture polystyrene (TCPS) cell culture plates. A total of 5×10^4 cells were added into each scaffold and allowed to incubate for 30 minutes, after which 1 ml media was added to each well. The scaffolds were incubated for 4 hours in conditions described earlier. Representative scaffolds in media with no cells from each group were tested in IVIS to confirm there was no non-specific bioluminescence. Empty seeded wells (media, no scaffolds) served as positive controls (N=6).

Cell proliferation on the scaffolds was tracked with the IVIS using the method described earlier on all scaffolds at 4 hours and daily through day 10. Luciferin was added to each well (150 μ g/ml) 5 minutes before imaging on auto exposure in the IVIS. An ROI was identified on each scaffold, from which Living Image was used to quantify luciferase expression in photons/second, and total cell counts on each scaffold was approximated using a standard curve derived from the data analyzed using GraphPad Prism software (GraphPad Software Inc., San Diego, CA, USA).

Cell counts for sintered and green groups and the control were plotted against time. Results were expressed as mean \pm SD for each group and were analyzed using analysis of variance (GraphPad Prism). For all tests, a p value of < 0.05 was considered statistically significant.

Cell morphology on the sintered HAp scaffolds was observed using SEM as described earlier. Scaffolds were fixed using a glutaraldehyde method [50]. Three to four images of the top face of each scaffold were taken at 5 kV to visualize representative cell morphology on the scaffolds.

Compression Testing

A screw-driven Tinius Olsen HIK-S UTM Benchtop Tester (Tinius Olsen, Horsham, PA, USA) equipped with a 1kN load cell was used to compression test the scaffolds until failure. Scaffold samples were prepared for testing by manually sanding the test surfaces using 1200 grit sandpaper to remove any protrusions and were measured to ensure the upper and lower faces were parallel. The samples were placed on an aluminum cross head and preloaded in compression to avoid slipping. Samples were tested in normal or transverse directions (Figure 1). Six samples were tested in each combination of porosity and direction. Compression tested sample groups are hereafter referred to as 60N, 60T, 70N, 70T, 80N, and 80T where the number is the designed porosity, and the letter denotes normal or transverse direction.

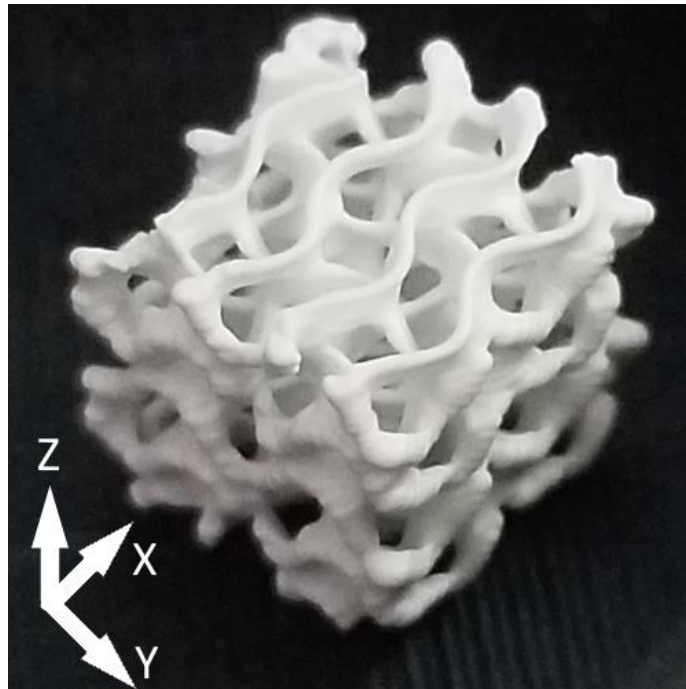


Figure 1: A printed 80% porous gyroid. The x-y plane is parallel with the scaffold build surface, i.e., the z-direction is the “height” axis. In normal testing, load is applied parallel with the z-axis, perpendicular to the x-y plane. In transverse testing, load is applied parallel with either the x-axis or y-axis, into the y-z or x-z planes, respectively.

The samples were loaded in compression at a 0.1mm/min crosshead speed and were video recorded to observe macroscopic failure. Failure was defined as the point where the applied load dropped to 75% from the peak load. Load and displacement were measured by the H1K-S and converted to stress and strain. The area used to calculate stress was derived by measuring each sample prior to testing and was assumed to be the nominal square cross-sectional area rather than the actual cross-sectional area (i.e., the presence of the designed porosity was not taken into account when calculating nominal stress). Ultimate compressive strength was defined as the peak stress recorded during each test. Compressive modulus was calculated using the initial linear region of the stress-strain response, as recorded by the H1K-S. We refer to this calculation as the “standard” compressive modulus. A second compressive modulus of the structure was additionally calculated for two cases. The first case uses the initial decrease in stress detectable on the stress-strain curve; the second case uses the maximum stress measured on the stress-strain curve. We refer to this calculation as the “construct” modulus. The standard method of measuring modulus (confined to the initial region of the stress-strain curve) can result in inaccurate values with cellular scaffolds due to initial failures of individual internal struts. Because of this, the actual effective modulus of the scaffold may be much higher. The additional measurement of a “construct” modulus was used to account for variations caused by initial failures within the scaffold. The brittle nature of the scaffolds leads to initial failures greatly affecting the elastic region of the stress-strain curve thereby altering the standard compressive modulus, even though the initial failure may ultimately prove to be insignificant in the overall load-bearing capacity of the scaffold. As shown later, this method reveals the effects of self-reinforcement occurring within the sample during failure. The compressive elastic modulus was calculated from the slope of these two charts and is hereafter referred to in this paper as either the

“first” or “peak” compressive construct modulus as this value is influenced by both material and structural properties rather than purely by material properties. Compression tests were recorded by video to enable identification of failure initiation and mode. The Weibull distribution was calculated in MATLAB using the two-parameter Weibull probability function [51], as defined in the following equation, where P is the probability of failure for a given stress (σ), m is the Weibull modulus, and σ_0 is a normalized stress value at which 1/e (~37%) of the samples survive.

$$P = 1 - \exp\left\{-\left(\frac{\sigma}{\sigma_0}\right)^m\right\}$$

Scanning Electron Microscopy

Scanning Electron Microscopy (SEM) on a JEOL JSM-6500F field emission scanning electron microscope (JEOL, Peabody, MA, USA) was utilized throughout the project to visualize internal sections of the scaffolds. Scaffold samples were first coated with 10nm of gold using a Denton Vacuum Desk II Gold Sputter Coater (Denton Vacuum, USA) and imaged at 15kV for all studies except cytotoxicity (below) which was imaged at 5kV. The SEM was equipped with an Oxford Instruments (Oxford Instruments, Abingdon, UK) energy dispersive X-ray spectrometer (EDS) for elemental composition and homogeneity analysis (described earlier) with site mapping and scanning performed using Oxford’s Aztec software.

Statistical Analysis

Statistical analysis was performed via the Analysis ToolPak Add-in for Microsoft Excel. Two-factor ANOVA (alpha=0.05) was used for comparing multiple sample sets. Comparisons

between specific sample sets were found by using a Two-Sample t-Test, assuming unequal variances, and using the two-tail test, with 95% confidence bounds ($p < 0.05$).

RESULTS

Rheological behavior, viscosity and homogeneity

Rheological behavior of 41 vol% HAp slurries is presented in log-log scale graphs. In figure 2 a significant decrease in the apparent viscosity (η) was observed as the shear rate ($\dot{\gamma}$) increased. Moreover, for 0.1 s^{-1} shear rate, an initial shear stress was necessary to begin deformation. These phenomena are typical of shear thinning fluids with viscoplastic behavior.

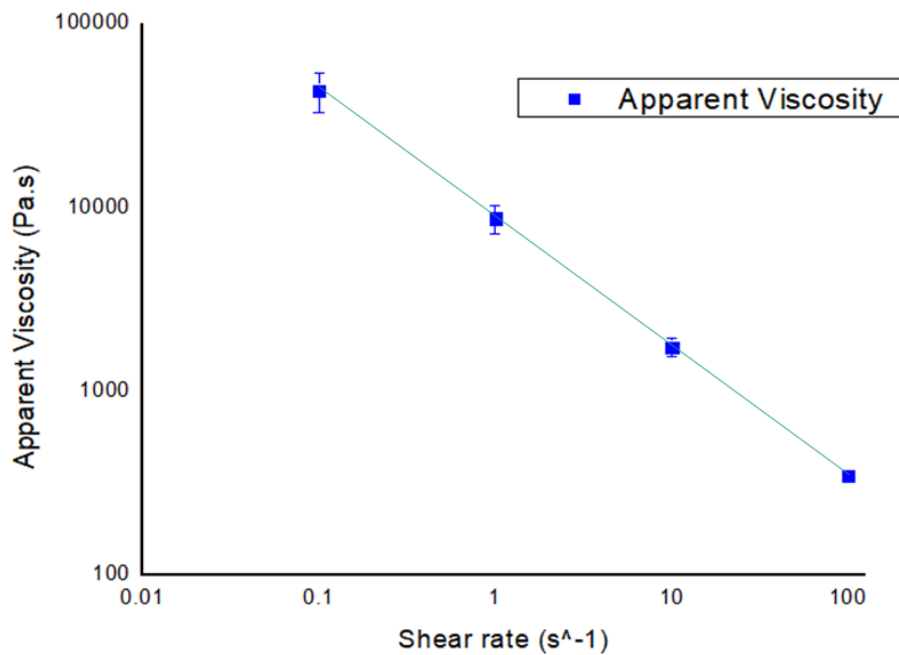


Figure 2: Shear rate vs Apparent Viscosity of the HAp slurry.

The apparent viscosity obtained by the different shear rates tested in a parallel plate setting obeyed the Ostwald de Waele (Power-Law) equation:

$$\eta = m(\dot{\gamma})^{n-1}$$

Where m represents the consistency of the slurry in units of MPa.s, and n is the power-law index of the shear thinning behavior of the fluid. The power-law index can take values between $0 < n < 1$ where the smaller the n value, the higher the shear thinning behavior of the fluid [52].

For 41 vol% HAp slurries, m and n values were $m = 9862.96 \pm 1610.23$ MPa.s and $n = 0.3 \pm 0.023$ with an $R^2 = 0.99 \pm 0.003$.

Figure 3 shows the rheological behavior of the HAp slurries as a function of storage time. For each shear rate, no significant difference was found ($p < 0.05$) in apparent viscosity for the days in which the measurements were taken. However, a small trend of increasing apparent viscosity is observed in figure 3, most noticeable on day 20. Hence, it was hypothesized based on the statistical analysis, that the storage conditions effectively prevented exposure to light, possible photopolymerization reaction and evaporation of EDGMA of HAp slurries, but they should be kept in storage for less than 20 days.

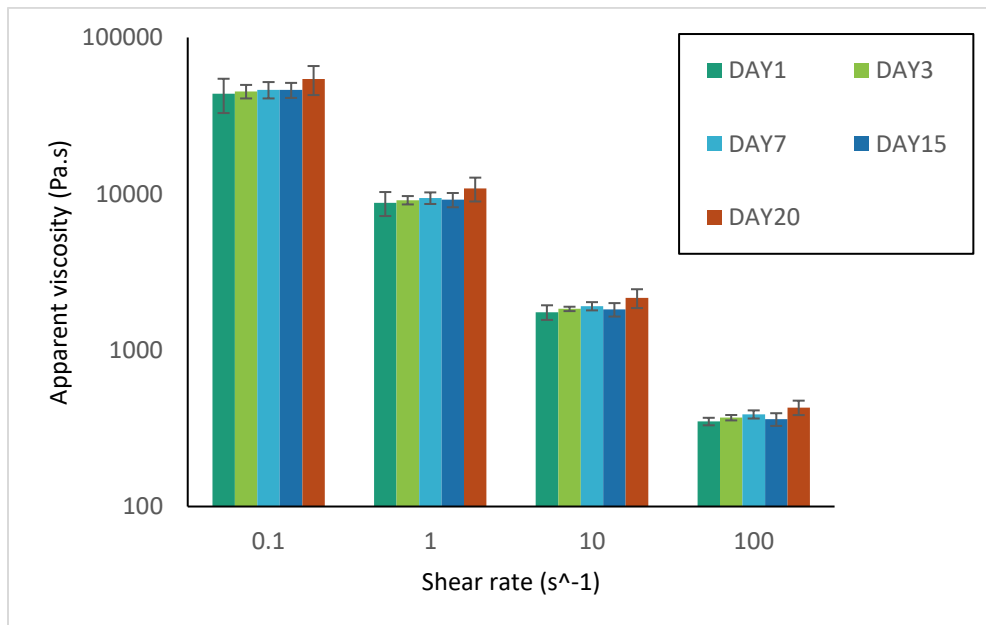


Figure 3: Shear rate vs Apparent Viscosity at different storage times.

Scaffold Dimensions & Shrinkage

Orientation of each sample was maintained to ensure each axis was being measured consistently, i.e., length (x-axis) measurements were always measured from the same faces of each scaffold. Average green scaffold dimensions differed from design by 0.6%-1.3%. The samples shrunk on average 20.48%-21.33% during sintering. Dimension and shrinkage results are recorded in Table 1.

Table 1: Scaffold Dimensions

	Length(x) (mm)	Width(y) (mm)	Height(z) (mm)
As-Designed	10	10	10
Green Scaffold	9.94 ± 0.09	9.87 ± 0.17	10.09 ± 0.05
Sintered Scaffold	7.89 ± 0.11	7.85 ± 0.06	7.95 ± 0.06
% Shrinkage	20.59 ± 1.93	20.48 ± 1.61	21.33 ± 0.77

Micro-CT: Total Volume, Filled Volume, Scaffold Porosity & Pore Size

Micro-CT results show that porosities of sintered scaffolds differed from designed porosities by 10.40%, 6.23%, and 3.5% for 60%, 70%, and 80% scaffolds, respectively. Mean spacing between roads differed by 1.34%, 0.73%, and 0.68%, respectively. Mean Total Volume, Mean Filled Volume, and Mean Spacing for all tested scaffolds are reported in Table 2.

Table 2: Results of micro-CT analysis.

Designed ϕ	60%	70%	80%
Mean TV (mm ³)	509.90	512.66	488.03
Mean FV (mm ³)	235.79	176.16	111.30
Mean ϕ (%)	53.76	65.64	77.19
$\Delta\phi$ (%)	6.24	4.36	2.81
Error (%)	10.40	6.23	3.51
Mean Spacing (mm)	0.55	0.71	1.23
Designed Spacing (mm)	0.49	0.76	1.31
Δ Spacing (mm)	0.06	0.05	0.08
Error (%)	1.34	0.73	0.68

TGA/EDS

Thermogravimetric analysis of green scaffold material revealed significant mass reduction at a rate of -1.174%/min beginning at approximately 250°C. This rate was consistent for 23.19 minutes. The final mass was 70.50% of the initial mass, indicating that 29.5% of material burned off during the test. The graph of this is presented in figure The TGA for sintered scaffold material over the same temperature range and ramp rate resulted in a mass loss of 0.05%. Graphs of both results can be seen in Figure 4.

Sample: test
Size: 51.5760 mg
Method: EHtest1

TGA

File: C:\...Emily\Downloads\green_scaffold.001
Operator: BSN
Run Date: 25-Oct-2019 14:01
Instrument: TGA Q500 V20.13 Build 39

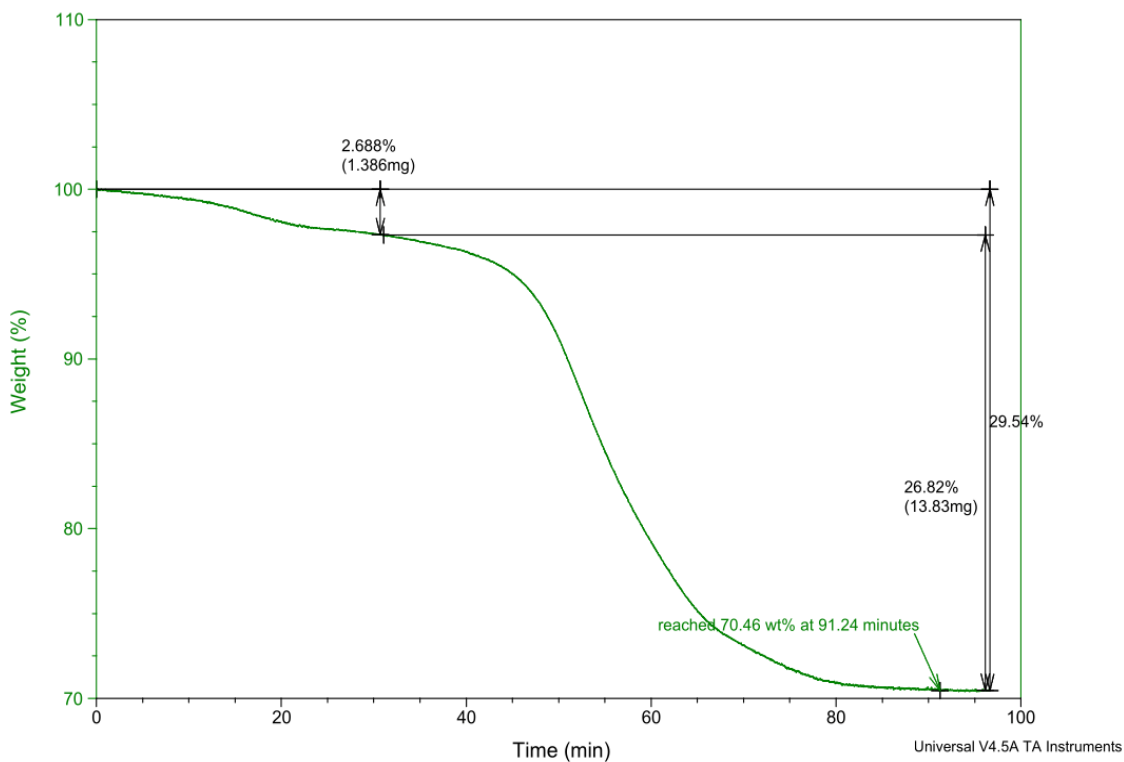


Figure 4: TGA results for green scaffold material.

Figure 5 shows a micrograph of the surface and elemental maps (EDS) of a green body of HAp. Equal distribution of oxygen, calcium, carbon, and phosphorus can be observed in the elemental maps through all the surface independent of surface roughness. Additionally, line scans were performed on the surface of the green scaffolds, and no significant changes in the characteristic emission of the elements were evident. This is shown in figure 6.

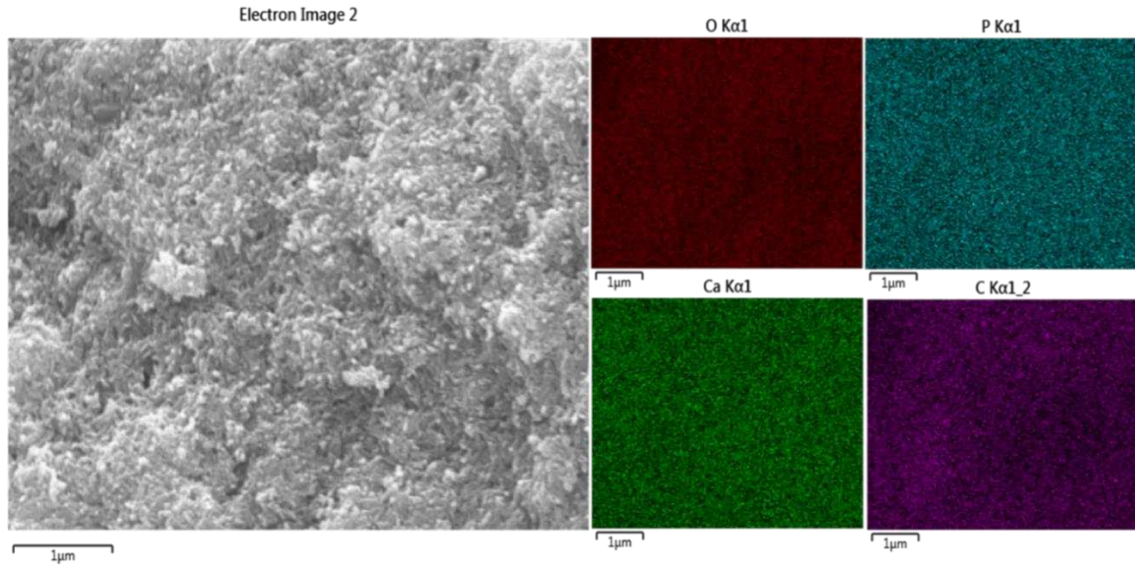


Figure 5: SEM of green body surface. EDS layered images of oxygen, phosphorous, calcium, and carbon are shown in the red, blue, green, and purple maps, respectively.

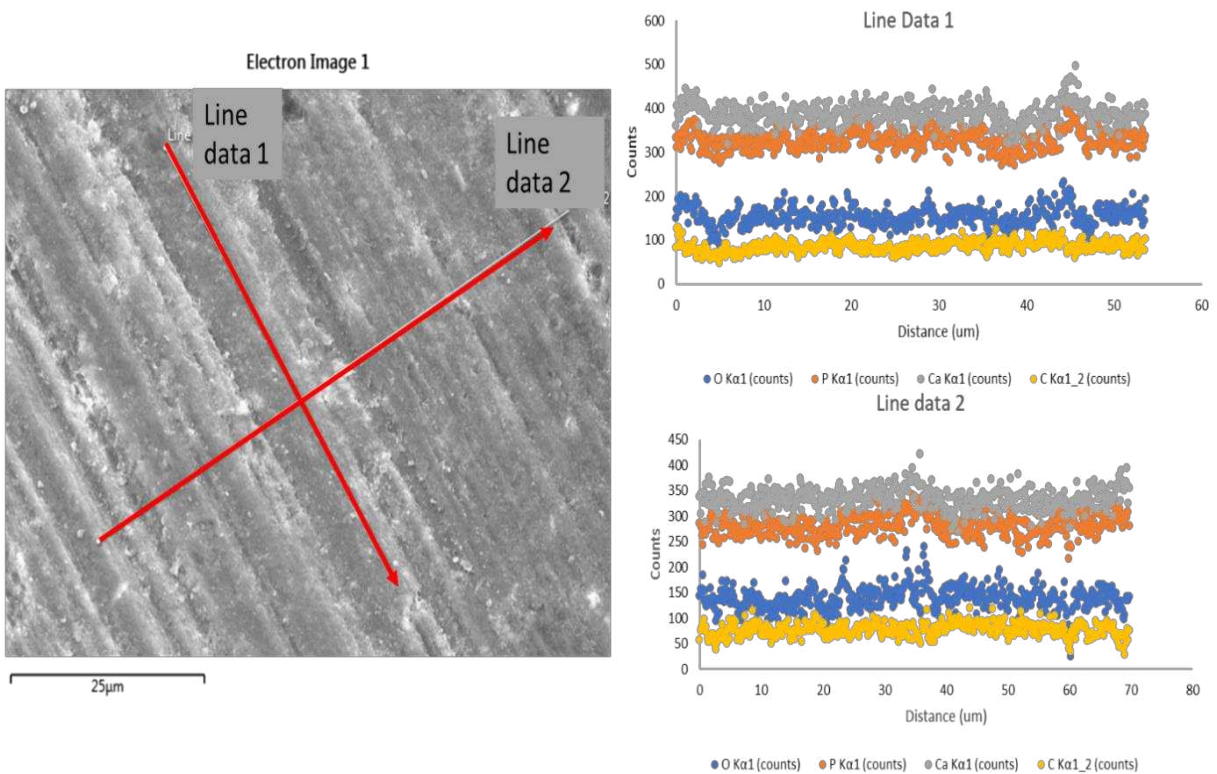


Figure 6: SEM of green body. EDS line scan paths shown in red. Line data results are shown on the right.

Cytotoxicity

Sintered HAp scaffolds are not cytotoxic to AD-MSC cells over a period of 10 days. PEGDMA/HAp green scaffolds (G) were cytotoxic at all timepoints (figure 8). All groups were significantly different between days 1 and 3. AD-MSC proliferation was significantly higher on sintered HAp scaffolds than on the TCPS control. Between days 4 and 7, the differences between ADSC proliferation on sintered HAp scaffolds and the TCPS control were not significant, but the sintered HAp scaffold had notably more cells than the TCPS control group. Between days 7 and 10, AD-MSC proliferation was significantly higher on sintered HAp scaffolds than on the TCPS control.

Compression Testing

Results for scaffold compression strengths are presented in Table 3. All sample sets were tested with $n=6$. The ultimate compressive strength in the normal direction is significantly higher (1.78 times) than when tested in the transverse direction for the same porosity. Ultimate compressive strengths are plotted in Figure 7 along with the minimum strength of cancellous bone. The Weibull moduli are between 3 and 6 with 70N showing an outlier of 1.68. Weibull distributions for each set are shown in Figure 8. Compressive construct moduli are similar for the 60% and 70% scaffolds and drop significantly for the 80% scaffolds. These values are presented in Table 4 and shown in Figure 9.

Table 3: Ultimate Compression Strength Results

Designed Porosity	60%	70%	80%	Weibull Modulus
Normal Ultimate Strength (MPa)	4.29 ± 0.45	1.96 ± 0.68	0.65 ± 0.13	6.13, 1.68, 5.72
Transverse Ultimate Strength (MPa)	2.34 ± 0.44	1.14 ± 0.18	0.36 ± 0.07	5.84, 3.38, 4.53

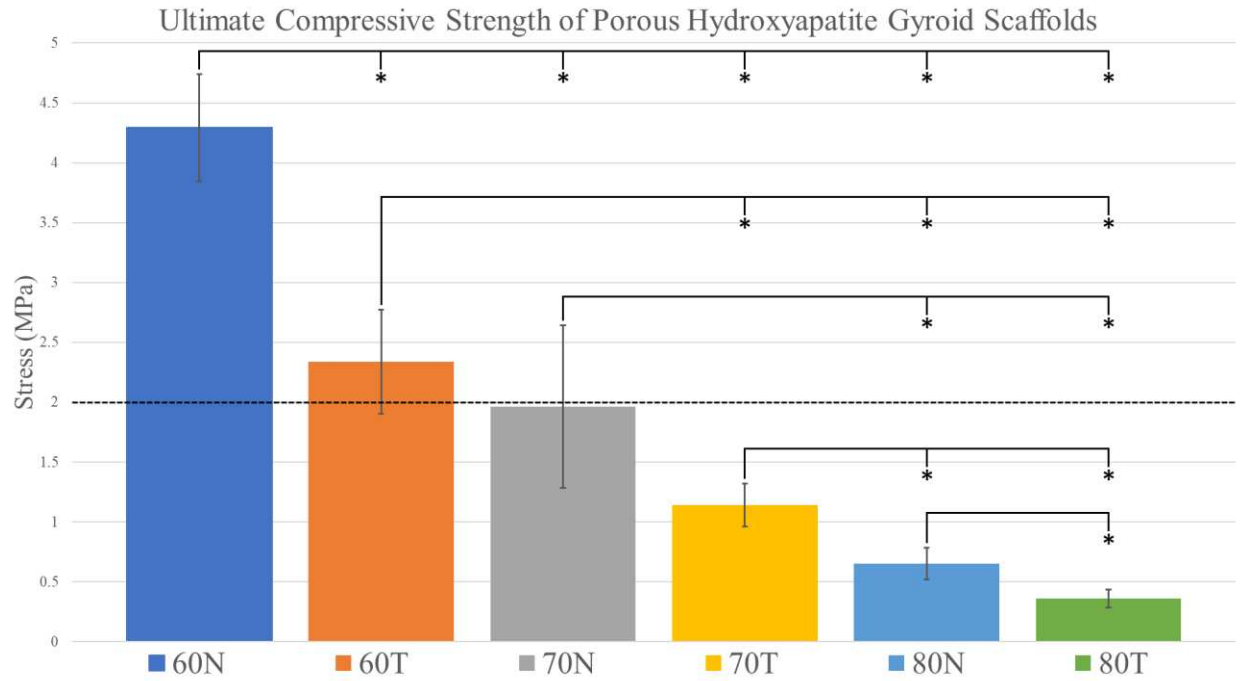


Figure 7: Ultimate compressive strength varies by porosity and direction. The dotted line denotes the lower limit of human cancellous bone strength. * = significantly different ($p > 0.05$).

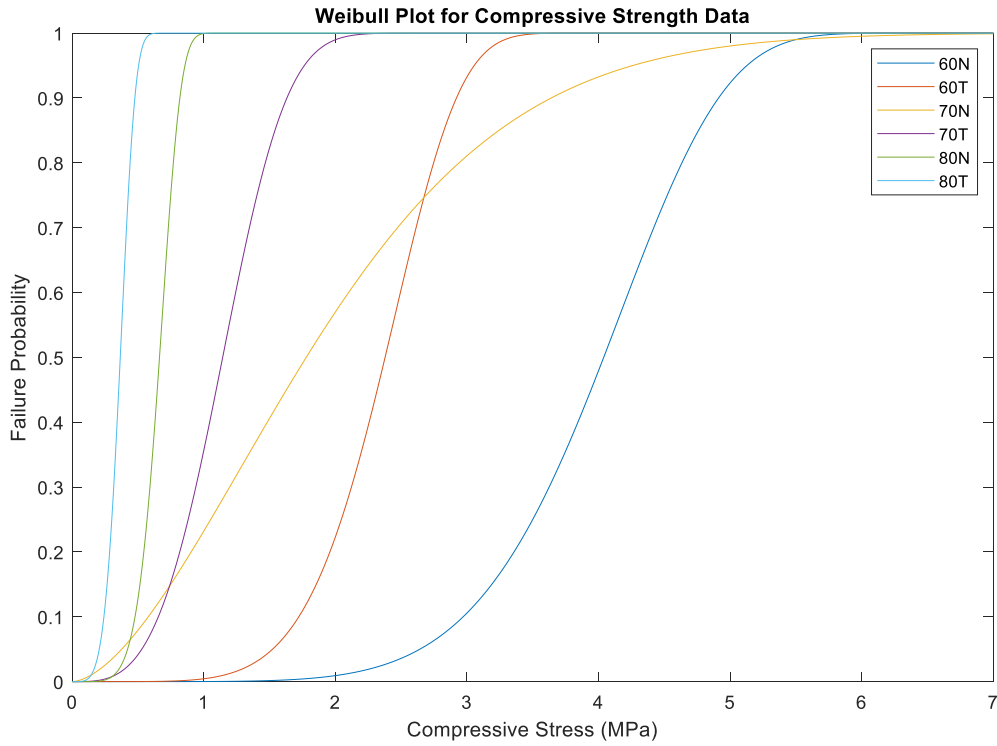


Figure 8: Failure probability for each scaffold set as determined via Weibull distribution. Steeper curves indicate more consistent failure stresses.

Table 4: Compression Modulus Results

Designed Porosity	60%	70%	80%
Normal Modulus (MPa)	76.30 ± 9.14	73.00 ± 8.00	43.35 ± 6.41
Transverse Modulus (MPa)	76.65 ± 8.55	83.01 ± 6.68	45.99 ± 6.17
Normal Standard Modulus (MPa)	63.82 ± 21.02	70.57 ± 16.42	42.01 ± 12.99
Normal First Modulus (MPa)	77.65 ± 18.08	74.62 ± 17.15	45.55 ± 14.9
Normal Peak Modulus (MPa)	87.43 ± 12.05	73.82 ± 17.46	42.50 ± 12.82
Transverse Standard Modulus (MPa)	76.52 ± 18.95	86.84 ± 13.05	49.32 ± 13.65
Transverse First Modulus (MPa)	77.09 ± 17.69	82.39 ± 12.48	46.71 ± 11.39
Transverse Peak Modulus (MPa)	79.33 ± 18.14	79.81 ± 12.89	41.93 ± 13.46

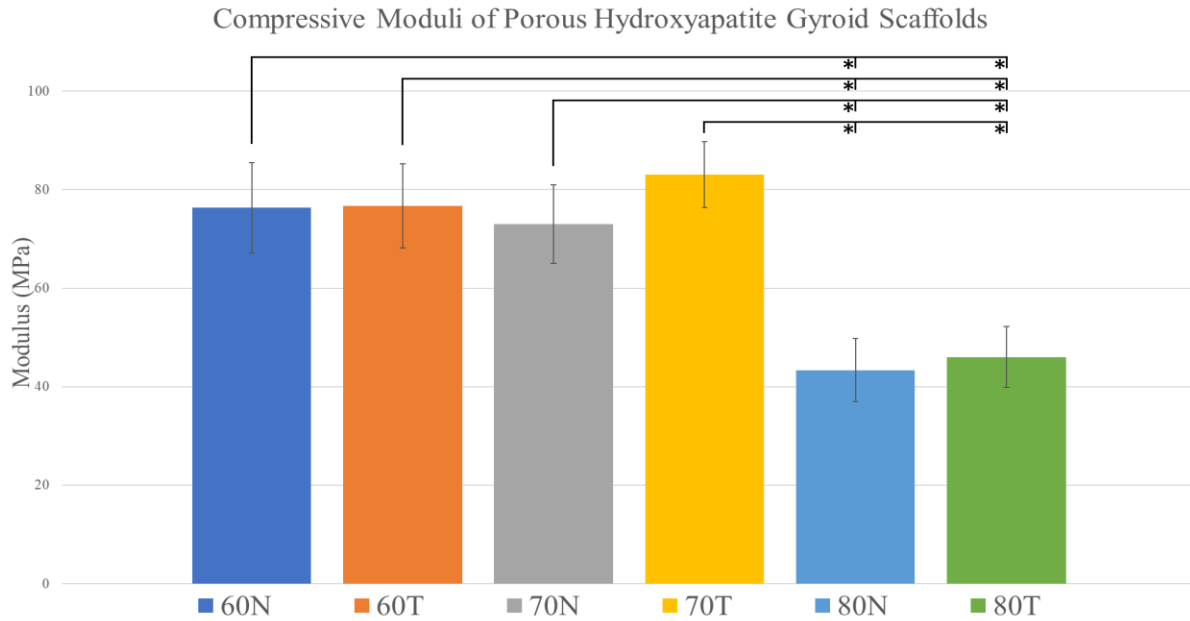


Figure 9: Compressive modulus remains similar for the 60% and 70% porous gyroids but is significantly lower for 80% porous scaffolds. * = significantly different ($p > 0.05$).

Failure Modes

Scaffold failure initiates at the surface cracks described earlier and progresses through the structure. This can be seen across the fracture surface of figure 10. Figure 10 also indicates that the cracks may continue travel across the internal road boundaries as local failure develops. Investigation of the surfaces resulting from failures indicate that the scaffolds primarily locally fail via intergranular fracture.

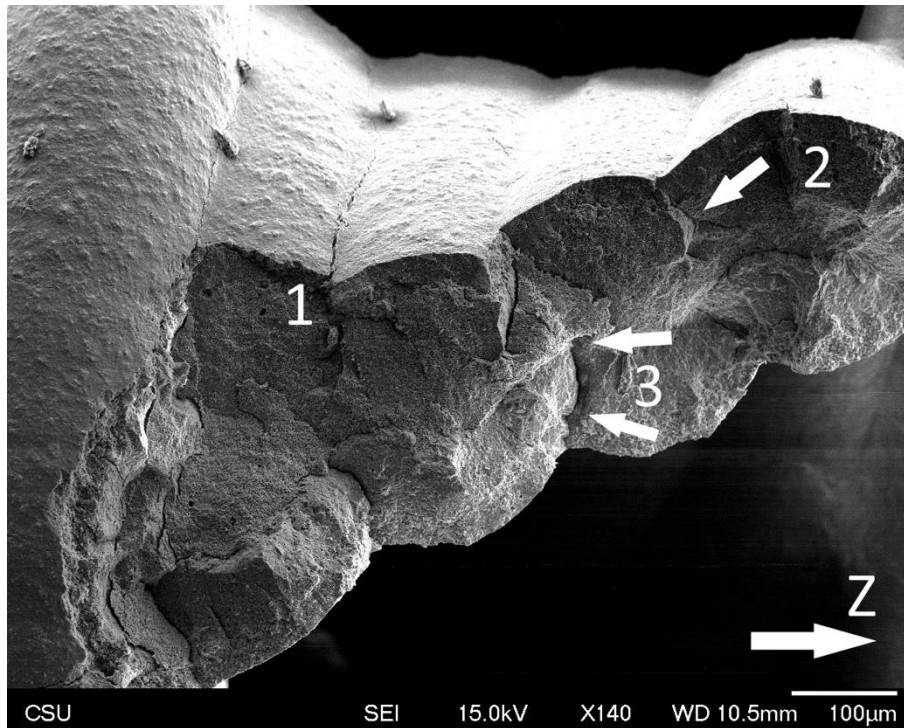


Figure 10: Fracture surface of a 70N scaffold. Location 1 shows a surface crack penetrating into the scaffold. Locations 2 and 3 show the crack progressing along the internal interface between roads.

Failure path and crack development was identified by reviewing recorded video footage of the testing. Example images taken from the videos can be seen in figure 11. Initial failure remained similar between all porosities and load directions. Deflection and deformation within the scaffolds were minimal as the material failed prior to any visible plastic deformation. We found that the path from local to global failure is affected by both porosity and loading direction. Generally, porosity influenced the global failure modes whereas loading direction influenced the local failure modes.

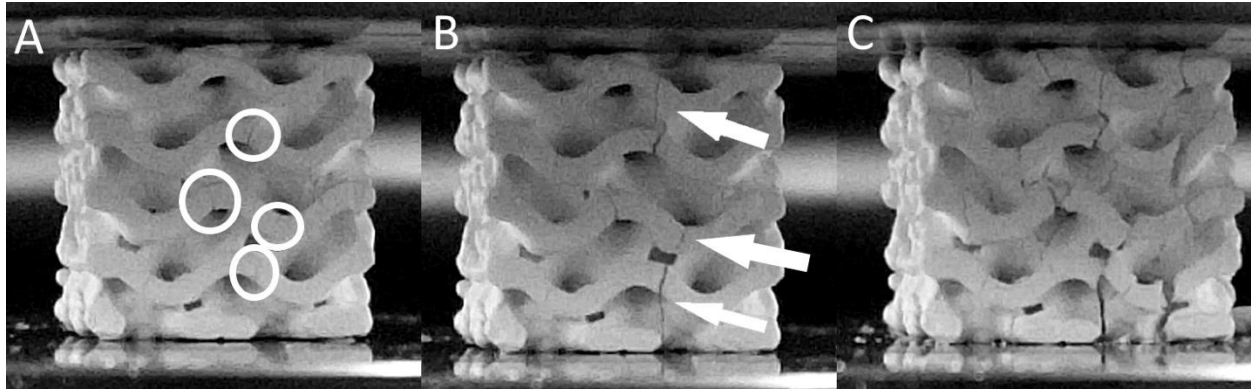


Figure 11: Failure path of an 80T sample from recorded video footage. A) The scaffold before loading. The circles indicate preexisting surface cracks. B) Initial failure of the scaffold. The preexisting cracks have propagated through the roads and are extending through the structure. C) Final failure of the scaffold. Cracks and local failures are present throughout the structure.

Our scaffolds show one of two types of porosity-dependent global failure. The scaffold either fails similarly to a monolithic structure or fails layer-by-layer. In monolithic failure, the stress rises through the initial elastic region, reaches the yield point, and the structure quickly fails afterwards with very little plastic deformation. In layer-by-layer failure, the stress also rises through a linear region before the first failure peak is identifiable. The curve drops sharply as the first layer failure progresses before rising again in subsequent layers as the material begins to self-reinforce against scaffold layers below it. This cycle of reinforcement repeats several times with decreasing local peak strengths before the scaffold ultimately fails. At 60% porosity, the scaffolds fail according to the first failure type. The stress-strain curves of the 70% porous scaffolds indicate a mixture of monolithic failure and layer-by-layer failure depending on the sample. The 80% porous scaffolds indicate high levels of layer-by-layer failure with lower peak to peak variability, suggesting self-reinforcement within the scaffolds. In several cases, the ultimate strength of the scaffold occurs after one or more local failures have already occurred. This correlation between porosity and failure mode has been identified in previous studies of gyroid structures [53].

DISCUSSION

Rheology

The viscosity of a slurry is dependent on the morphology of the dispersed phase; thus, the asymmetric needle-like particles likely affect the consistency of the slurry. The more the particles deviate from spherical symmetry, the more the viscosity increases because asymmetric particles gain more kinetic energy that dissipates with the applied force that resulted from the shear rate [54]. This has an obvious effect on 3D printability, especially of complex structures, as discussed later. While this effect confounded our ability to determine printing parameters, ultimately it did not play a significant role in consistent fabrication of our scaffolds after ideal parameters were determined. The variability in the consistency (m) in the Ostwald de Waele equation presented earlier could be a result of the temperature change in the room at the moment of testing, and the resistance of the needle-like HAp particles to flow.

Comparing As-Designed and As-Built Scaffolds

Slight variation between printed part and CAD model is expected due to minor inconsistencies in printing slurry-based materials. This variation arises fundamentally because the shear-thinning behavior of the slurry as it is being extruded through the nozzle leads to variations in flow behavior. This is most noticeable in the reduction in porosity between as-printed and as-designed scaffolds (Table 2). The reduction in relative porosity from the as-designed values is believed to result from small inconsistencies in slurry flow during the printing process. These variations are caused by small amounts of material that extrude due to back pressure while the print head is traveling between print locations. The plunger that drives the extrusion is backed off slightly during head movement to decrease this back pressure within the syringe, but small amounts of

material continue to flow toward the nozzle tip during these head movements. This causes variation in as-printed dimensionality and as-printed road width, both of which contribute to variation in porosity. Future work might consider using a clench valve to mitigate this effect. This effect is noticeable in the micro-CT images (Figure 12). As expected, it is most pronounced in the roads facing the exterior of each scaffold (the perimeters) where the extrusion starts and stops but can be identified in the interior of the scaffold as well.

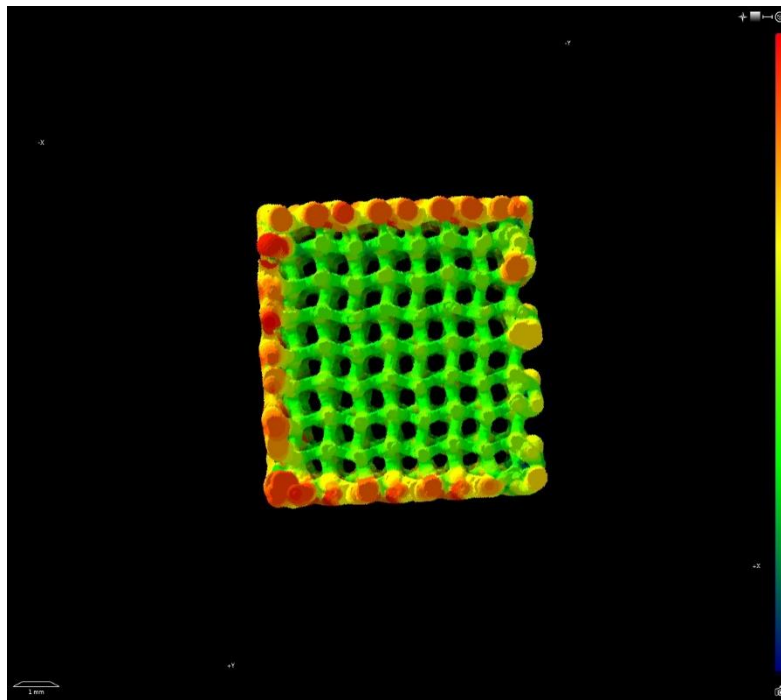


Figure 12: Micro-CT imaging of a 60% porous scaffold. Green regions indicate nominal material thickness, orange regions indicate greater material thickness.

Our gyroid scaffolds experienced isotropic shrinkage when sintered at 1200°C. Each dimension was reduced by 20.5%~21.25% and no significant difference was found between directions or porosities. Previous work with this material reported isotropic shrinkage of $15.92 \pm 0.95\%$ for fully dense HAp samples sintered at 1150°C [47]. The additional shrinkage is theorized to be from two primary causes. First is the higher sintering temperature. The ideal sintering temperature for a HAp-based structure has been repeatedly investigated and identified to be

within a similar range (1100-1350°C) and is highly dependent on the method used to produce the structure [55]–[58]. Generally, methods that produce a more microporous material require a higher temperature to fully densify the structure. The material used in this work achieves higher density at 1200°C compared to 1150°C (78.90% to 73.5%, respectively) [47]. This further densification leads to additional shrinkage. Secondly, gyroid structures experience more uniform heating than the fully dense structures. The interconnected porous channels throughout the scaffold create a much higher surface area and allow for heat transfer throughout the scaffold compared to the more limited surface area of fully dense rectangular prisms used in the prior study. This leads to more uniform densification of the material and higher shrinkage overall.

TGA/EDS

TGA results of green scaffold material indicate near-complete pyrolysis of the organic components at before reaching 500°C, confirming prior thermogravimetric analysis of our material [47]. Sintered material decreased by only 0.05% during the test. This confirmation is necessary to show that the organic components are completely removed from the scaffold material during sintering.

EDS results demonstrate that HAp was evenly dispersed in EDGMA in our fabrication process and that the homogeneous dispersion was maintained after printing the structures. Pressure applied by the syringe plunger in the 3D printing process was not enough to break the electrosteric forces created by D540. Thus, HAp particles do not agglomerate and clog the nozzle and maintain the dispersion in the printed structures after 3D printing.

Cytotoxicity

Decreased AD-MSK proliferation observed in the first day is a normal and expected result of some number of cells failing to attach to the scaffolds, but which were able to attach to the TCPS. The decrease in AD-MSK proliferation after day 6 on both sintered HAp scaffolds and the TCPS control group appears to be due to the cells becoming confluent earlier than expected. The negative impact of confluence is lower on sintered HAp scaffolds than on the TCPS control group, likely because there is much more internal surface area available in the three-dimensional structure of the scaffolds than on the two-dimensional bottom of a TCPS well. The AD-MSKs were able to spread out much more in the 3D internal surfaces of the scaffolds, while still being detected by the IVIS camera.

Scaffold Consistency

Curing depth is affected by the opaque nature of the slurry, as hydroxyapatite particles quickly block the UV light from penetrating deeper into the material [59]. This difference in curing is theorized to lead to additional material discontinuities in the final structure. During sintering concentric cracks form within the rod, in some cases appearing as a ring of near-complete delamination of peripheral material from material closer to the core. An example can be seen in figure 13.

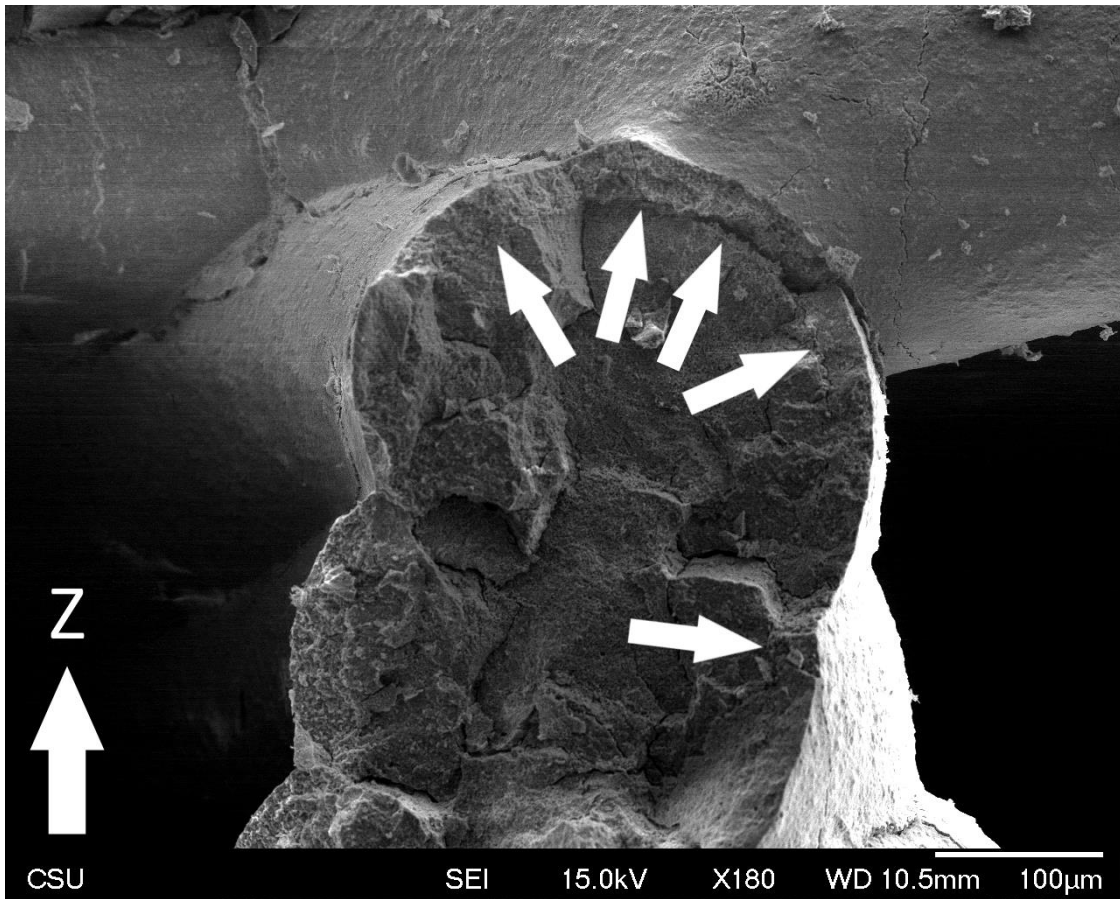


Figure 13: Fracture surface of a 60N scaffold. The arrows point towards the concentric ring present along the roads. The ring is delaminating in the upper-right corner of the exposed surface.

In cases where the concentric ring does not fully separate from the core material, relief cracks can be seen extending from the ring/core interface (Figure 14). For reference, the Z direction is the build direction. The thickness of the outer ring is thought to be correlated with the thickness of the fully cured region, but this was not evaluated. Increasing the power of the UV light, implementing additional light sources, and utilizing a dedicated curing box with self-contained omnidirectional high intensity UV light all failed to prevent formation of the concentric crack. This led to two theories: the first is that the material opacity is simply too high to allow for thorough curing, the second theory is that thermal stresses associated with sintering are causing the concentric cracks. It is hypothesized that the actual cause is a combination of the two, that the

thermal expansion properties of the material change as the effective curing decreases. This difference causes internal stress as material expands/contracts; the material reacts at different rates, leading to internal stress and eventual local fracture within the printed road. This would explain why the concentric cracks consistently appear at a depth of approximately 25 μm , as this is the depth where the curing decreases sufficiently enough for the thermal expansion differences to begin thermally shielding the interior material, thus creating a thermal gradient that increases the internal stress within the printed material.

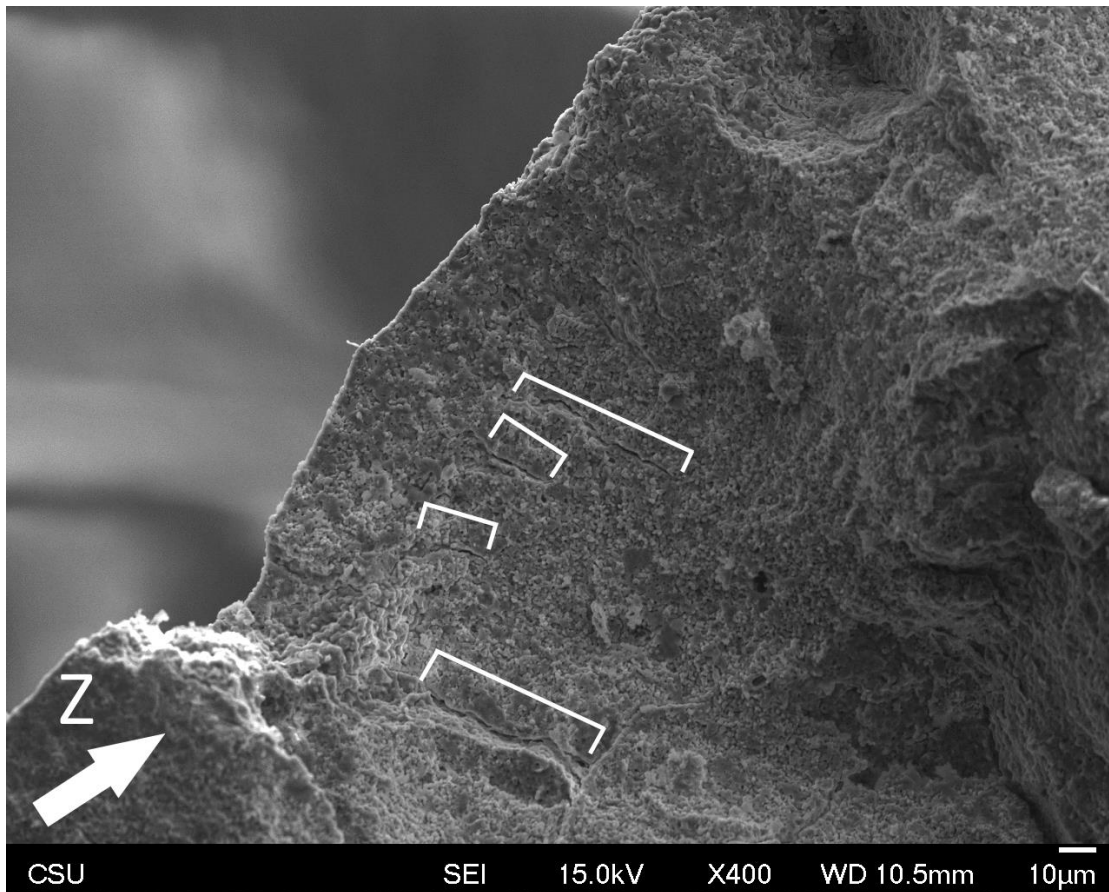


Figure 14: Fracture surface of an 80N scaffold. Interior cracks extend from the concentric ring towards the core of the road.

The scaffolds contain cracks both across the external surfaces and in the internal sections of printed roads throughout the structure. Surface cracks form primarily along the surface where

two roads intersect. These cracks initiate at the surface and appear to penetrate the scaffold as failure progresses (discussed later) along the interfacial boundary between the roads. Uncured material is being extruded over cured material in the previous layer and simultaneously cured. We hypothesize that as it cures it does not bond completely with the previous surface, which is already cured. As sintering progresses, thermal stresses increase as temperatures rise within the road and the difference in material property resulting from different levels of curing disrupts the materials' thermal expansion and acts as a stress concentrator. The point where the two roads meet then becomes the site of a surface crack as the material attempts to dissipate this energy.

Compressive Strength/ Construct Modulus

It has previously been demonstrated in rectilinear scaffolds with porosities of 55%-75% that relative porosity does not significantly affect the mechanical response of a scaffold [60]. Our work demonstrates that with photocast hydroxyapatite gyroid scaffolds the ultimate compression strength varied significantly between different porosities. The relationship between porosity and compressive strength is consistent for both normal (to the build platform) and transverse directions: the ratio of each is shown in Table 4. These findings confirm our hypothesis that the gyroid topology provides additional strength at any porosity, exceeding the strength improvement that would be realized due to the addition of more material. If the amount of material in the structure was the sole factor affecting compressive strength, then a 60% porous scaffold should be twice as strong as an 80% porous scaffold as it contains twice as much material. In Table 4, this is referred to as the theoretical ratio. In fact, a 60% porous scaffold is 6.6x (in the normal direction) or 6.45x (transverse) stronger than an 80% porous scaffold. These values are referred to as experimental ratios in Table 4.

Table 4: Ultimate Compression Strength Ratios

Ratio	60%/70%	70%/80%	60%/80%
Normal, Theoretical Ratio	1.33	1.5	2
Normal, Experimental Ratio	2.19	3.02	6.60
Normal, Experimental/ Theoretical	1.65	2.01	3.30
Transverse, Theoretical Ratio	1.33	1.5	2
Transverse, Experimental Ratio	2.05	3.15	6.45
Transverse, Experimental/ Theoretical	1.54	2.10	3.23

Example from this table: the theoretical strength ratio of 60%/80% is 2, assuming the amount of material (and thus area the stress is applied across) is the only modifying factor, since the 60% scaffold has twice the material (per design parameters) as the 80% scaffold. The experimental ratio is the mean ultimate compressive strength of the 60N scaffolds divided by the 80N scaffolds; in this case, the ratio of 60N/80N is 6.60. Therefore, the experimental/theoretical ratio is 3.30 and the increase in strength is 3.30x of the expected value.

At each porosity value, the scaffolds survived significantly higher loads when tested in the z-direction (Figure 1) compared to those tested in the transverse direction. While it is well-understood that the strengths of additively manufactured parts vary with loading direction, often the transverse direction is the stronger because the printed material is aligned with the loading direction [61]. In this case, however, the transverse direction is significantly weaker than the normal direction. Upon closer inspection of the printed parts, this difference in strength appears to be due to the overlapping material between layers. Since material is deposited layer-wise, slightly offset from the road below it, material in a new road has a larger than designed

interfacial area with a previous rod. This increases strength when loaded in the normal direction, as this overlap allows for greater dispersal of force throughout the scaffold as noted in recent published literature regarding PLA gyroids [62].

Failure in ceramic materials is highly dependent on internal flaws (discussed later) and therefore the strength of ceramic structures is dependent on the distribution of these flaws. While many distributions exist, the Weibull distribution and the Weibull modulus are the most widely used method for determining the variability of strengths in ceramic materials [63], [64]. The Weibull modulus of our scaffolds, with one exception, are in the range of the low end of engineering ceramics ($m = 5-20$) [65]. Previously published literature has shown that solid (no relative porosity) HAp specimens with microporosity between 51% and 62% exhibit Weibull modulus values of 8~15 [66]. In comparison, the macroporous scaffolds in this work exhibit Weibull moduli in the range of approximately $m = 3-6$. While lower, these moduli are still in the low range of engineering ceramics and are thus suitably predictable for use in designed structures. This range also falls within the range of rectilinear macroporous HAp and β -TCP scaffolds found in other works [33], [67].

The 70N (70% porosity, normal test) scaffolds, where the Weibull modulus was found to be 1.68, highlight the variability of ceramic materials. The results of compression testing 70N had the highest variance of any data set and therefore decreased the Weibull modulus appropriately. This reduction in result consistency is theorized to be a result of the limited sample size ($n=6$). Additional tests with larger sample sizes are recommended in order to determine if the range in values is accurate and to avoid representation bias due to differences in batches of test samples [68]–[70].

The Weibull failure probability graph (Figure 8) can be used to predict the failure mode of the scaffolds. The 60% porous scaffolds tend to experience monolithic failure with less self-reinforcement and thus greater variability in results; this is reflected in the Weibull failure graph. Conversely, the 80% porous scaffolds exhibit high rates of self-reinforcement. This leads to less variability in failure results and a much narrower failure plot. It is therefore our hypothesis that developing scaffolds which exclusively fail layer-by-layer will ultimately yield more mechanically consistent scaffolds.

The compressive construct modulus remained largely consistent between the 60% and 70% porous scaffolds. No combination of measurements between test groups is significantly different ($p < 0.05$). The 80% porous scaffolds, however, displayed markedly lower compressive moduli than the others. In context of the consistency between the 60% and 70% porous scaffolds, this significant drop in compressive modulus would indicate a critical porosity value above which the compressive modulus drops dramatically. Other work, involving polymeric materials [17], has found similar decreases in modulus as porosity increases although in a different range of porosity than reported in this work.

In self-reinforcing structures, measuring the compressive modulus using our alternate method (the construct modulus) results in values comparable to the standard measurement of structures that do not suffer initial failures. Examples of these different cases can be seen in Figure 15. In more than half of our tests, such as in a), the H1K-S value and the subsequent values align closely. In cases such as b), c), and d), initial failures and subsequent changes in the stress-strain slope led to early measurements of the compressive modulus when the effective value may in fact be higher or lower. These measurements combine to create a defined range of an effective modulus for the structure.

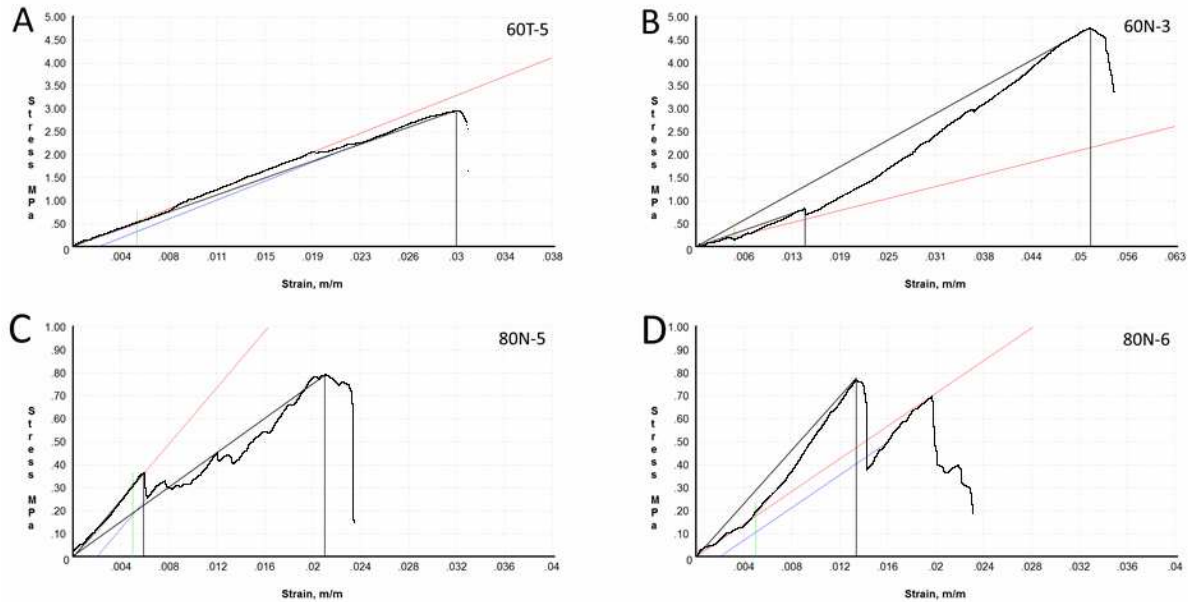


Figure 15: Representative moduli. Red = as measured. Black vertical line = manual measurement. A) Measurements align closely. B) Early failure - standard modulus < effective modulus. C) Effective modulus < standard modulus. D) Self-reinforcement after initial failure – second phase of the curve has a modulus similar to the first phase

It is difficult to compare our results to other robocast gyroid HAp scaffolds because publications on this specific scaffold type are difficult to find. However, we can compare our scaffolds to other HAp-based structures. Rectilinear 55% porous robocast HAp scaffolds developed by Cox et al. [71] recorded peak compressive strengths of 0.88 MPa. Lee et al. [72] recently published a study using digital light processing (photopolymerization) to fabricate 70% porous HAp gyroid scaffolds that reached a peak ultimate compressive strength of 11.5 ± 1.75 MPa. It is worth noting that photopolymers are usually cytotoxic, and this study did not evaluate cytotoxicity.

The standard compressive moduli measured for our 60% and 70% porous sample groups were between 73 MPa and 83 MPa and compare favorably with recent work using porous HAp structures. Jin et al. [73] created 70% gyroid PLA/ β -TCP/HAp scaffolds with a mean modulus of approximately 15 MPa. Huang et al. [74] achieved a comparable compressive moduli of 75.72 using PCL/HAp with a denser (50% porous) rectilinear scaffold structure.

Failure Modes

As is typical for ceramic materials and further corroborated by a Weibull distribution fit of ultimate compressive strengths, the failure modes of our scaffolds were found to be highly flaw dependent. When tested in the normal direction, each scaffold suffered initial fractures corresponding to the initial crack sites like those shown in Figure 11. The progression from surface cracks to fracture can be seen in still frames taken from video footage (see Supplemental Material for an instance of this). Upon fracture of the rod, the now-broken piece remains lodged against the neighboring material rather than dislocating, much like an architectural arch. This can be observed in Figure 16 as well as visually in tested scaffolds. This can also be seen in the stress-strain curves for these tests, as several saw-tooth patterns can be seen through the curve. This behavior is encouraging; it indicates that an implant produced with our topology and material that exceeds its yield stress, when loaded in the normal direction, would likely maintain its integrity beyond initial failure of individual struts, thus enabling subsequent loading and bone growth at the site. After experimental measurements were completed, the scaffolds maintained their integrity after the crosshead was returned to its initial position. However, immediately upon removing the scaffold from the crosshead, the scaffolds broke apart into numerous individual pieces.

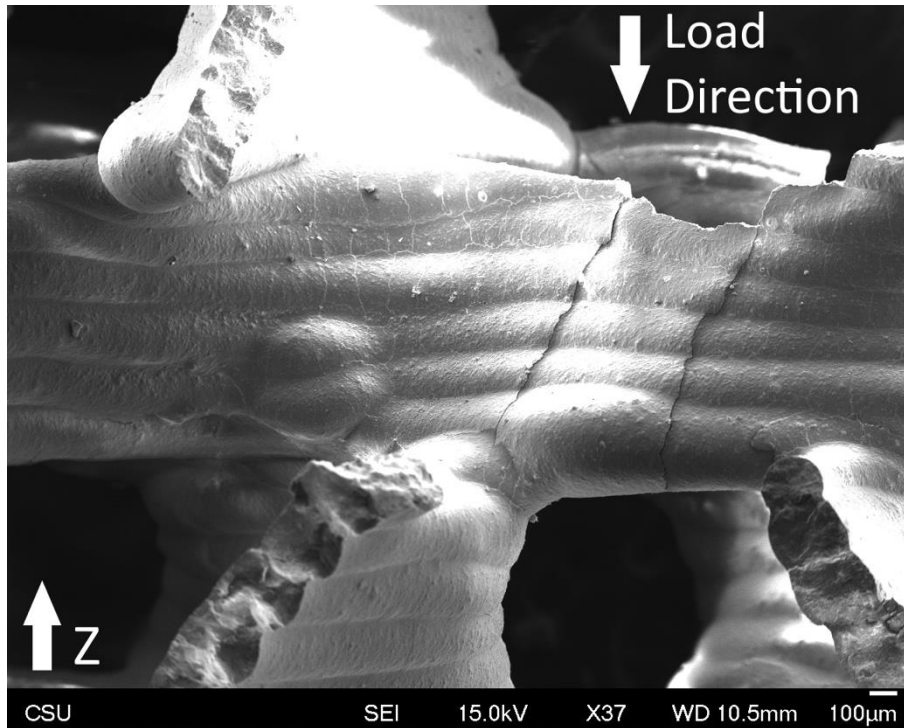


Figure 16: A section of an 80N showing a failed section reinforced against neighboring material.

When tested in the transverse direction, the structure also exhibited self-reinforcing behavior but to a significantly lesser extent than the scaffolds tested normally. This can be seen in the stress strain curves, as the initial stress peaks are generally followed by an immediate stress decrease until the material begins reinforcing itself. In the transverse loading direction, initial local failures cause the material to displace and separate from the remainder of the material before becoming lodged in other sections of the scaffold, similarly to what was observed in the normal direction scaffolds. However, the sections appear to be less likely to fully lodge into place compared to when tested in the normal direction, resulting in lesser self-reinforcement. Transverse-tested scaffolds also maintained their integrity following removal from the crosshead; however, like the normally loaded scaffolds, they immediately collapsed when touched. The surface cracks discussed earlier have a significantly higher effect in transverse direction loading than in normal loading. Cracks that appear on the surface follow the interfacial boundary

between the roads. When the scaffold is loaded transversely, this boundary provides an opportunity for each road to shift and deform. This deformation causes local bending, which induces tension in the ceramic roads, which in turn causes the material to fail at significantly lower loads than when under compression. These cracks can be seen in figure 17. This leads to earlier initial local failure and results in formation of additional sites for cracks to progress.

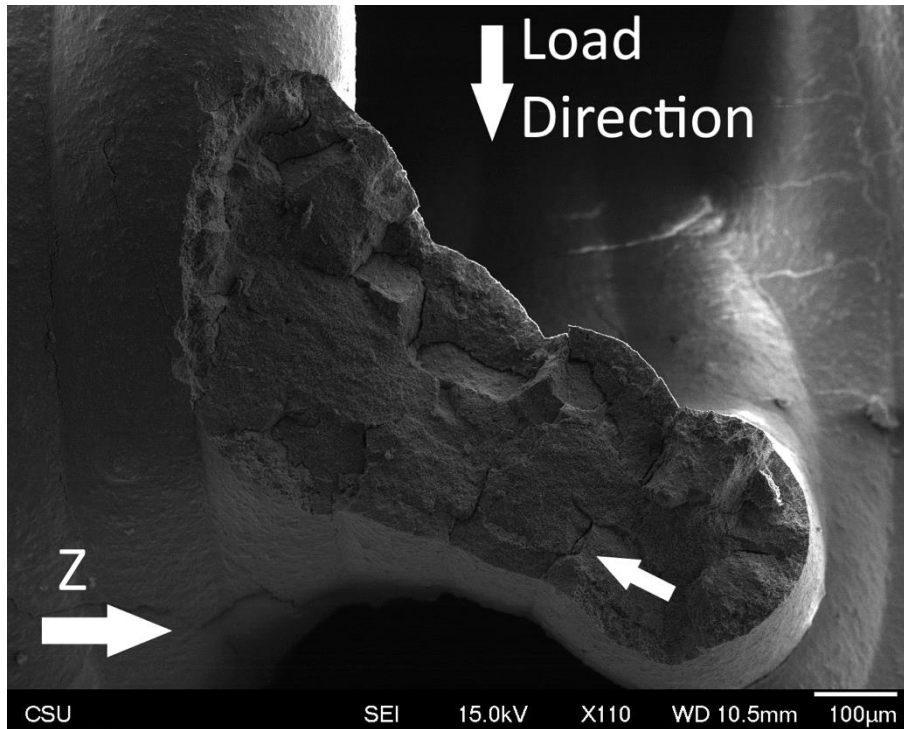


Figure 17: Failure surface of a 70N scaffold. Note that the surface cracks penetrate each road interface along the side of the scaffold strut that experiences tension in this scenario, whereas the surface cracks along the compression side appear less organized.

It is our belief that the presence of the surface cracks is the most influential factor limiting the strength of these scaffolds. HAp has been reported as being particularly vulnerable to crack growth, even compared to ceramics as a whole [75], [76]. Other work has reported compressive strengths and compressive moduli significantly higher than those reported here. A common theme amongst those works is deployment of a method of limiting or eliminating the cracks. The gyroid HAP scaffolds in Lee et al. [72], for example, were sintered in a slower multi-step

process, produced fewer defects, and resulted in significantly stronger scaffolds. Crack propagation is highly dependent on the grain size and the density of the material. Smaller grain sizes, and therefore more grain boundaries, delay the progression of the crack by causing the crack to deflect around the grain thereby increasing material strength [77]. The density and grain size of AM ceramic materials is greatly but indirectly influenced by the sintering process [58]. Higher sintering temperatures and hold times allow greater densification as well as additional grain growth. This leads to conflicting effects, as the higher level of density will increase the mechanical strength, whereas the larger grains will begin to weaken the material. The grain size effect is described in the Hall-Petch equation; though initially developed for polycrystalline metals, published work has shown that the Hall-Petch relationship is applicable to dense ceramics as well as dense HAp [78]–[82].

$$\sigma_{yt} = \sigma_0 + \frac{k_y}{\sqrt{d}} \quad EQ 3$$

where k_y is the Hall-Petch slope and d is the grain size. The Hall-Petch slope is a constant and is determined empirically. From this equation, as grain size decreases, the strength increases. This equation involves the yield strength rather than ultimate strength; given the brittle nature of the structures, however, the yield strength and ultimate strength seldom differ. In order to minimize grain growth, lower sintering temperatures and/or hold times are required. Conversely, lower temperatures lead to lower density as the micropores are not fully removed at the lower temperatures. A change from of only 50°C, from 1200°C to 1150°C in the same ramp and hold times, decreases the material density from 78.90% to 73.50% due to lack of coalescence of the micropores [47]. The surface HAp grains and the internal micropores between HAp grains of a structure sintered at 1200°C can be seen in figure 18. These micropores contribute significantly

to local fracture modes in the structure. Therefore, our material benefits from higher sintering temperatures, though an unknown temperature limit where the effects reverse exists. Similar conclusions have been found in other research as well [83], [84].

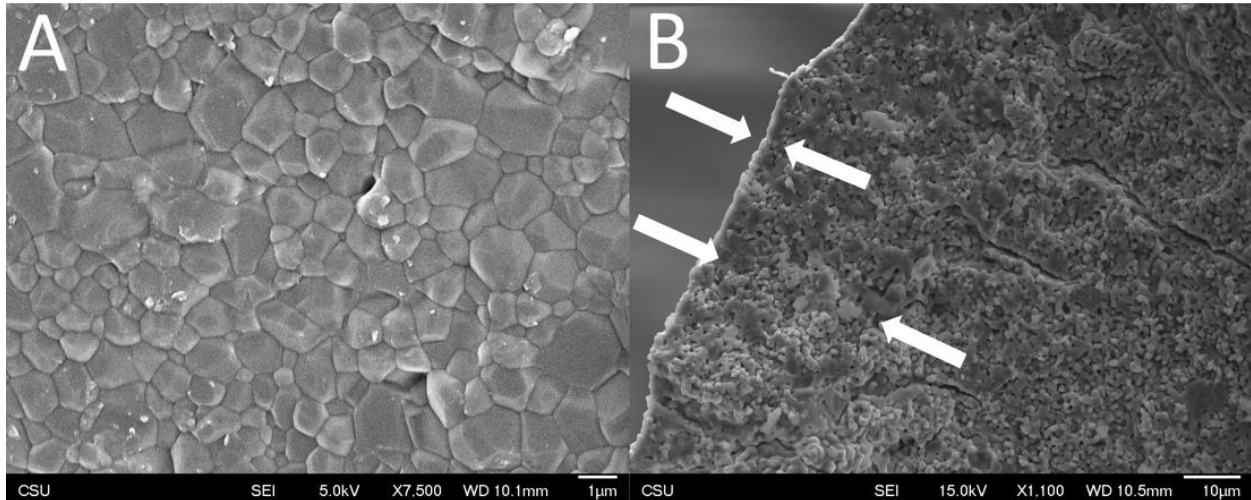


Figure 18: SEM of a sintered scaffold. A) shows the fully densified surface grains. B) shows the micropores between HAp grains. The dense surface grains extend approximately 0.5-2 μm into the road, as shown with the narrower arrow region. The concentric ring is marked by the larger span of arrows.

CONCLUSIONS

We were able to successfully design, fabricate, and test hydroxyapatite gyroid scaffolds using a layer-wise, photopolymerized viscous extrusion additive manufacturing method we refer to as photocasting. Gyroids and other complex structures can be easily, accurately and precisely printed using photocasting. Our work confirms that gyroid structures impart greater compressive strengths on scaffolds than would be expected based on material characteristics alone. Our 60%-70% porous, photocast, HAp gyroid scaffolds have sufficient compressive strength to serve as cancellous bone grafts. Micro-CT analysis confirms the interconnected topology of all pores in the scaffolds. Cytotoxicity experiments confirm that our scaffolds are non-cytotoxic. Our scaffolds failed in a manner consistent with a “leak-before-break” design philosophy, where

initial local failures do not immediately cause catastrophic full-scale failure. This allows some regions of the gyroid scaffold to fail while others maintain the overall integrity of the device, potentially enhancing the efficacy of the scaffold *in vivo*. Additional research into toughness and further verification of compressive strengths is required to ensure that the scaffolds could fully mechanically suffice as cancellous bone grafts. While our tests were limited to representative sections of gyroid architecture, their mechanical response is enticing enough to warrant additional investigation and research into utilizing larger scale structures based on these gyroid unit cells and functional grading of gyroid and related topologies. If these mechanical responses remain consistent and are shown to be scalable properties, then these gyroid unit cell structures could prove valuable as artificial bone grafts in the future.

REFERENCES

- [1] Meddevicetracker, “US. Markets for Orthopedic Biologic and Tissue Engineering Products,” Informa PLC, London, ENGLAND, MedTech Analysis Report A428, May 2015. [Online]. Available: <https://pharmastore.informa.com/product/u-s-markets-for-orthopedic-biologic-and-tissue-engineered-products/>
- [2] J. Henkel *et al.*, “Bone Regeneration Based on Tissue Engineering Conceptions — A 21st Century Perspective,” *Bone Res.*, vol. 1, no. 3, pp. 216–248, Sep. 2013, doi: 10.4248/BR201303002.
- [3] V. Viateau *et al.*, “A technique for creating critical-size defects in the metatarsus of sheep for use in investigation of healing of long-bone defects,” *American Journal of Veterinary Research*, vol. 65, no. 12, pp. 1653–1657, Dec. 2004, doi: 10.2460/ajvr.2004.65.1653.
- [4] D. Chang and K. Weber, “Use of a vascularized fibula bone flap and intercalary allograft for diaphyseal reconstruction after resection of primary extremity bone sarcomas,” *Plast Reconstr Surg*, vol. 116, pp. 1918–1925, 2005.
- [5] V. Viateau *et al.*, “Long-bone critical-size defects treated with tissue-engineered grafts: A study on sheep,” *J. Orthop. Res.*, vol. 25, no. 6, pp. 741–749, Jun. 2007, doi: 10.1002/jor.20352.
- [6] L. Vidal, C. Kamplaitner, M. Á. Brennan, A. Hoornaert, and P. Layrolle, “Reconstruction of Large Skeletal Defects: Current Clinical Therapeutic Strategies and Future Directions Using 3D Printing,” *Front. Bioeng. Biotechnol.*, vol. 8, p. 61, Feb. 2020, doi: 10.3389/fbioe.2020.00061.
- [7] S. Bhumiratana *et al.*, “Tissue-engineered autologous grafts for facial bone reconstruction,” *Sci. Transl. Med.*, vol. 8, no. 343, pp. 343ra83–343ra83, Jun. 2016, doi: 10.1126/scitranslmed.aad5904.
- [8] J. L. Vondran, W. Sun, and C. L. Schauer, “Crosslinked, electrospun chitosan–poly (ethylene oxide) nanofiber mats,” *Journal of Applied Polymer Science*, vol. 109, pp. 968–975, 2008.
- [9] S. Bose, S. Vahabzadeh, and A. Bandyopadhyay, “Bone tissue engineering using 3D printing,” *Materials Today*, vol. 16, no. 12, pp. 496–504, Dec. 2013, doi: 10.1016/j.mattod.2013.11.017.
- [10] Q. Zhang, W. Wang, E. Schmelzer, J. Gerlach, C. Liu, and I. Nettleship, “The degradation behavior of calcium-rich hydroxyapatite foams in vitro,” *Journal of Biomedical Materials Research Part A*, vol. 109, no. 6, pp. 859–868, 2021, doi: <https://doi.org/10.1002/jbm.a.37077>.
- [11] J. Liuyun, X. Chengdong, J. Lixin, and X. Lijuan, “Effect of hydroxyapatite with different morphology on the crystallization behavior, mechanical property and in vitro degradation of hydroxyapatite/poly(lactic-co-glycolic) composite,” *Composites Science and Technology*, vol. 93, pp. 61–67, Mar. 2014, doi: 10.1016/j.compscitech.2013.12.026.
- [12] S. Bose, D. Ke, H. Sahasrabudhe, and A. Bandyopadhyay, “Additive manufacturing of biomaterials,” *Progress in Materials Science*, vol. 93, pp. 45–111, Apr. 2018, doi: 10.1016/j.pmatsci.2017.08.003.
- [13] H. Montazerian, E. Davoodi, M. Asadi-Eydivand, J. Kadkhodapour, and M. Solati-Hashjin, “Porous scaffold internal architecture design based on minimal surfaces: A compromise

- between permeability and elastic properties,” *Materials & Design*, vol. 126, pp. 98–114, Jul. 2017, doi: 10.1016/j.matdes.2017.04.009.
- [14] H. Montazerian, M. Zhianmanesh, E. Davoodi, A. S. Milani, and M. Hoorfar, “Longitudinal and radial permeability analysis of additively manufactured porous scaffolds: Effect of pore shape and porosity,” *Materials & Design*, vol. 122, pp. 146–156, May 2017, doi: 10.1016/j.matdes.2017.03.006.
- [15] F. P. W. Melchels, K. Bertoldi, R. Gabbrielli, A. H. Velders, J. Feijen, and D. W. Grijpma, “Mathematically defined tissue engineering scaffold architectures prepared by stereolithography,” *Biomaterials*, vol. 31, no. 27, pp. 6909–6916, Sep. 2010, doi: 10.1016/j.biomaterials.2010.05.068.
- [16] S. C. Kapfer, S. T. Hyde, K. Mecke, C. H. Arns, and G. E. Schröder-Turk, “Minimal surface scaffold designs for tissue engineering,” *Biomaterials*, vol. 32, no. 29, pp. 6875–6882, Oct. 2011, doi: 10.1016/j.biomaterials.2011.06.012.
- [17] D. W. Abueidda, M. Elhebeary, C.-S. (Andrew) Shiang, S. Pang, R. K. Abu Al-Rub, and I. M. Jasiuk, “Mechanical properties of 3D printed polymeric Gyroid cellular structures: Experimental and finite element study,” *Materials & Design*, vol. 165, p. 107597, Mar. 2019, doi: 10.1016/j.matdes.2019.107597.
- [18] L. Yuan, S. Ding, and C. Wen, “Additive manufacturing technology for porous metal implant applications and triple minimal surface structures: A review,” *Bioactive Materials*, vol. 4, no. 1, pp. 56–70, Mar. 2019, doi: 10.1016/j.bioactmat.2018.12.003.
- [19] L. Germain, C. A. Fuentes, and A. W. van Vuure, “3D-printed biodegradable gyroid scaffolds for tissue engineering applications,” *Materials and Design*, p. 10, 2018.
- [20] K. C. R. Kolan, A. Thomas, M. C. Leu, and G. Hilmas, “*In vitro* assessment of laser sintered bioactive glass scaffolds with different pore geometries,” *Rapid Prototyping Journal*, vol. 21, no. 2, pp. 152–158, Mar. 2015, doi: 10.1108/RPJ-12-2014-0175.
- [21] M. Alizadeh-Osgouei, Y. Li, A. Vahid, A. Ataee, and C. Wen, “High strength porous PLA gyroid scaffolds manufactured via fused deposition modeling for tissue-engineering applications,” *Smart Materials in Medicine*, vol. 2, pp. 15–25, Jan. 2021, doi: 10.1016/j.smaim.2020.10.003.
- [22] Castro, Pires, Santos, Gouveia, and Fernandes, “Permeability versus Design in TPMS Scaffolds,” *Materials*, vol. 12, no. 8, p. 1313, Apr. 2019, doi: 10.3390/ma12081313.
- [23] F. P. W. Melchels, A. M. C. Barradas, C. A. van Blitterswijk, J. de Boer, J. Feijen, and D. W. Grijpma, “Effects of the architecture of tissue engineering scaffolds on cell seeding and culturing,” *Acta Biomaterialia*, vol. 6, no. 11, pp. 4208–4217, Nov. 2010, doi: 10.1016/j.actbio.2010.06.012.
- [24] J. Santos, T. Pires, B. P. Gouveia, A. P. G. Castro, and P. R. Fernandes, “On the permeability of TPMS scaffolds,” *Journal of the Mechanical Behavior of Biomedical Materials*, vol. 110, p. 103932, Oct. 2020, doi: 10.1016/j.jmbbm.2020.103932.
- [25] F. Liu, Z. Mao, P. Zhang, D. Z. Zhang, J. Jiang, and Z. Ma, “Functionally graded porous scaffolds in multiple patterns: New design method, physical and mechanical properties,” *Materials & Design*, vol. 160, pp. 849–860, Dec. 2018, doi: 10.1016/j.matdes.2018.09.053.
- [26] A. P. G. Castro, J. Santos, T. Pires, and P. R. Fernandes, “Micromechanical Behavior of TPMS Scaffolds for Bone Tissue Engineering,” *Macromol. Mater. Eng.*, vol. 305, no. 12, p. 2000487, Dec. 2020, doi: 10.1002/mame.202000487.
- [27] M. Bahraminasab, “Challenges on optimization of 3D-printed bone scaffolds,” *BioMed Eng OnLine*, vol. 19, no. 1, p. 69, Dec. 2020, doi: 10.1186/s12938-020-00810-2.

- [28] ASTM TC261 Committee, “52900:2015(E) Additive manufacturing — General principles — Terminology,” ASTM, Dec. 2015. [Online]. Available: <https://www.iso.org/standard/69669.html>
- [29] N. Travitzky *et al.*, “Additive Manufacturing of Ceramic-Based Materials: Additive Manufacturing of Ceramic-Based Materials,” *Advanced Engineering Materials*, vol. 16, no. 6, pp. 729–754, Jun. 2014, doi: 10.1002/adem.201400097.
- [30] E. Peng, D. Zhang, and J. Ding, “Ceramic Robocasting: Recent Achievements, Potential, and Future Developments,” *Adv. Mater.*, vol. 30, no. 47, p. 1802404, Nov. 2018, doi: 10.1002/adma.201802404.
- [31] X. Lv, F. Ye, L. Cheng, S. Fan, and Y. Liu, “Binder jetting of ceramics: Powders, binders, printing parameters, equipment, and post-treatment,” *Ceramics International*, vol. 45, no. 10, pp. 12609–12624, Jul. 2019, doi: 10.1016/j.ceramint.2019.04.012.
- [32] C. Schmidleithner, S. Malferrari, R. Palgrave, D. Bomze, M. Schwentenwein, and D. M. Kalaskar, “Application of high resolution DLP stereolithography for fabrication of tricalcium phosphate scaffolds for bone regeneration,” *Biomed. Mater.*, vol. 14, no. 4, p. 045018, Jun. 2019, doi: 10.1088/1748-605X/ab279d.
- [33] Martinez-Vazquez, F. *et al.*, “Effect of Polymer Infiltration on the Flexural Behavior of β -Tricalcium Phosphate Robocast Scaffolds,” *Materials*, vol. 7, pp. 4001–4018, 2014.
- [34] Houmard, M. *et al.*, “On the structural, mechanical, and biodegradation properties of HA β -TCP robocast scaffolds.pdf,” *J. Biomed. Mater. Res. - Part B Appl. Biomater.*, vol. 101, pp. 1233–1242, May 2013, doi: 10.1002/jbm.b.32935.
- [35] S. Eqtesadi, A. Motealleh, A. Pajares, F. Guiberteau, and P. Miranda, “Improving mechanical properties of 13–93 bioactive glass robocast scaffold by poly (lactic acid) and poly (ϵ -caprolactone) melt infiltration,” *Journal of Non-Crystalline Solids*, vol. 432, pp. 111–119, Jan. 2016, doi: 10.1016/j.jnoncrysol.2015.02.025.
- [36] H. Jin, Y. Zhuo, Y. Sun, H. Fu, and Z. Han, “Microstructure design and degradation performance in vitro of three-dimensional printed bioscaffold for bone tissue engineering,” *Advances in Mechanical Engineering*, vol. 11, no. 10, Art. no. 10, Oct. 2019, doi: 10.1177/1687814019883784.
- [37] J. W. Halloran, “Ceramic Stereolithography: Additive Manufacturing for Ceramics by Photopolymerization,” *Annual Review of Materials Research*, vol. 46, no. 1, pp. 19–40, Jul. 2016, doi: 10.1146/annurev-matsci-070115-031841.
- [38] M. Pfaffinger, M. Hartmann, M. Schwentenwein, and J. Stampfl, “Stabilization of tricalcium phosphate slurries against sedimentation for stereolithographic additive manufacturing and influence on the final mechanical properties,” *Int J Appl Ceram Technol*, vol. 14, no. 4, pp. 499–506, Jul. 2017, doi: 10.1111/ijac.12664.
- [39] A. Zocca, P. Colombo, C. M. Gomes, and J. Günster, “Additive Manufacturing of Ceramics: Issues, Potentialities, and Opportunities,” *Journal of the American Ceramic Society*, vol. 98, no. 7, pp. 1983–2001, Jul. 2015, doi: 10.1111/jace.13700.
- [40] M. Faes, H. Valkenaers, F. Vogeler, J. Vleugels, and E. Ferraris, “Extrusion-based 3D Printing of Ceramic Components,” *Procedia CIRP*, vol. 28, pp. 76–81, 2015, doi: 10.1016/j.procir.2015.04.028.
- [41] M. Asif *et al.*, “A new photopolymer extrusion 5-axis 3D printer,” *Additive Manufacturing*, vol. 23, pp. 355–361, Oct. 2018, doi: 10.1016/j.addma.2018.08.026.
- [42] R. D. Farahani, L. L. Lebel, and D. Therriault, “Processing parameters investigation for the fabrication of self-supported and freeform polymeric microstructures using ultraviolet-

- assisted three-dimensional printing,” *J. Micromech. Microeng.*, vol. 24, no. 5, p. 055020, 2014, doi: 10.1088/0960-1317/24/5/055020.
- [43] S.-W. Choi, Y. Zhang, and Y. Xia, “Three-Dimensional Scaffolds for Tissue Engineering: The Importance of Uniformity in Pore Size and Structure,” *Langmuir*, vol. 26, no. 24, pp. 19001–19006, Dec. 2010, doi: 10.1021/la104206h.
- [44] S. C. Cowin and L. Cardoso, “Blood and interstitial flow in the hierarchical pore space architecture of bone tissue,” *Journal of Biomechanics*, vol. 48, no. 5, pp. 842–854, Mar. 2015, doi: 10.1016/j.jbiomech.2014.12.013.
- [45] S. Van Bael *et al.*, “The effect of pore geometry on the in vitro biological behavior of human periosteum-derived cells seeded on selective laser-melted Ti6Al4V bone scaffolds,” *Acta Biomaterialia*, vol. 8, no. 7, pp. 2824–2834, Jul. 2012, doi: 10.1016/j.actbio.2012.04.001.
- [46] J. Will *et al.*, “Porous ceramic bone scaffolds for vascularized bone tissue regeneration,” *J Mater Sci: Mater Med*, vol. 19, no. 8, pp. 2781–2790, Aug. 2008, doi: 10.1007/s10856-007-3346-5.
- [47] Lopez Ambrosio, Katherine V., “HYDROXYAPATITE STRUCTURES CREATED BY ADDITIVE MANUFACTURING WITH EXTRUDED PHOTOPOLYMER,” Master’s Thesis, Colorado State University, Ft. Collins, CO, 2019.
- [48] M. E. Aanstoos, D. P. Regan, R. J. Rose, L. S. Chubb, and N. P. Ehrhart, “Do Mesenchymal Stromal Cells Influence Microscopic Residual or Metastatic Osteosarcoma in a Murine Model?,” *Clin Orthop Relat Res*, vol. 474, no. 3, pp. 707–715, Mar. 2016, doi: 10.1007/s11999-015-4362-2.
- [49] J. L. Sottnik, D. L. Duval, E. J. Ehrhart, and D. H. Thamm, “An orthotopic, postsurgical model of luciferase transfected murine osteosarcoma with spontaneous metastasis,” *Clin Exp Metastasis*, vol. 27, no. 3, pp. 151–160, Mar. 2010, doi: 10.1007/s10585-010-9318-z.
- [50] B. S. Smith, S. Yoriya, L. Grissom, C. A. Grimes, and K. C. Popat, “Hemocompatibility of titania nanotube arrays,” *J. Biomed. Mater. Res.*, vol. 95A, no. 2, pp. 350–360, Jul. 2010, doi: 10.1002/jbm.a.32853.
- [51] M. F. Burrow, D. Thomas, M. V. Swain, and M. J. Tyas, “Analysis of tensile bond strengths using Weibull statistics,” *Biomaterials*, vol. 25, no. 20, pp. 5031–5035, Sep. 2004, doi: 10.1016/j.biomaterials.2004.01.060.
- [52] R. P. Chhabra, “Non-Newtonian Fluids: An Introduction,” in *Rheology of Complex Fluids*, J. M. Krishnan, A. P. Deshpande, and P. B. S. Kumar, Eds. New York, NY: Springer New York, 2010, pp. 3–34. doi: 10.1007/978-1-4419-6494-6_1.
- [53] M. Keshavarzan, M. Kadkhodaei, M. Badrossamay, and M. R. Karamooz Ravari, “Investigation on the failure mechanism of triply periodic minimal surface cellular structures fabricated by Vat photopolymerization additive manufacturing under compressive loadings,” *Mechanics of Materials*, vol. 140, p. 103150, Jan. 2020, doi: 10.1016/j.mechmat.2019.103150.
- [54] K. Holmberg, D. O. Shah, and M. J. Schwuger, Eds., *Handbook of applied surface and colloid chemistry*. Chichester, England ; New York: Wiley, 2002.
- [55] S. Ramesh *et al.*, “Sintering properties of hydroxyapatite powders prepared using different methods,” *Ceramics International*, vol. 39, no. 1, pp. 111–119, Jan. 2013, doi: 10.1016/j.ceramint.2012.05.103.

- [56] V. Jokanović *et al.*, “Kinetics and sintering mechanisms of hydro-thermally obtained hydroxyapatite,” *Materials Chemistry and Physics*, vol. 111, no. 1, Art. no. 1, Sep. 2008, doi: 10.1016/j.matchemphys.2008.04.005.
- [57] G. Muralithran and S. Ramesh, “The effects of sintering temperature on the properties of hydroxyapatite,” *Ceramics International*, vol. 26, no. 2, pp. 221–230, Mar. 2000, doi: 10.1016/S0272-8842(99)00046-2.
- [58] O. Prokopiev and I. Sevostianov, “Dependence of the mechanical properties of sintered hydroxyapatite on the sintering temperature,” *Materials Science and Engineering: A*, vol. 431, no. 1–2, pp. 218–227, Sep. 2006, doi: 10.1016/j.msea.2006.05.158.
- [59] J. W. Halloran *et al.*, “Photopolymerization of powder suspensions for shaping ceramics,” *Journal of the European Ceramic Society*, vol. 31, no. 14, pp. 2613–2619, Nov. 2011, doi: 10.1016/j.jeurceramsoc.2010.12.003.
- [60] J. Russias *et al.*, “Fabrication and in vitro characterization of three-dimensional organic/inorganic scaffolds by robocasting,” *J. Biomed. Mater. Res.*, vol. 83A, no. 2, pp. 434–445, Nov. 2007, doi: 10.1002/jbm.a.31237.
- [61] P. Miranda, A. Pajares, and F. Guiberteau, “Finite element modeling as a tool for predicting the fracture behavior of robocast scaffolds,” *Acta Biomaterialia*, vol. 4, no. 6, pp. 1715–1724, Nov. 2008, doi: 10.1016/j.actbio.2008.05.020.
- [62] M. Alizadeh-Osgouei, Y. Li, A. Vahid, A. Ataei, and C. Wen, “High strength porous PLA gyroid scaffolds manufactured via fused deposition modeling for tissue-engineering applications,” *Smart Materials in Medicine*, vol. 2, pp. 15–25, 2021, doi: 10.1016/j.smaim.2020.10.003.
- [63] S. F. Duffy, L. M. Powers, and A. Starlinger, “Reliability Analysis of Structural Ceramic Components Using a Three-Parameter Weibull Distribution,” *Journal of Engineering for Gas Turbines and Power*, vol. 115, no. 1, pp. 109–116, Jan. 1993, doi: 10.1115/1.2906664.
- [64] J. J. Petrovic, “Weibull statistical fracture theory for the fracture of ceramics,” *Metall Mater Trans A*, vol. 18, no. 11, pp. 1829–1834, Nov. 1987, doi: 10.1007/BF02647012.
- [65] J. Gong and Y. Li, “Relationship between the Estimated Weibull Modulus and the Coefficient of Variation of the Measured Strength for Ceramics,” *Journal of the American Ceramic Society*, vol. 82, no. 2, pp. 449–452, 1999, doi: <https://doi.org/10.1111/j.1551-2916.1999.tb20084.x>.
- [66] X. Fan, E. D. Case, F. Ren, Y. Shu, and M. J. Baumann, “Part I: Porosity dependence of the Weibull modulus for hydroxyapatite and other brittle materials,” *Journal of the Mechanical Behavior of Biomedical Materials*, vol. 8, pp. 21–36, Apr. 2012, doi: 10.1016/j.jmbbm.2011.12.010.
- [67] P. Miranda, A. Pajares, E. Saiz, A. P. Tomsia, and F. Guiberteau, “Mechanical properties of calcium phosphate scaffolds fabricated by robocasting,” *J. Biomed. Mater. Res.*, vol. 85A, no. 1, pp. 218–227, Apr. 2008, doi: 10.1002/jbm.a.31587.
- [68] A. D. Papargyris, “Estimator type and population size for estimating the weibull modulus in ceramics,” *Journal of the European Ceramic Society*, vol. 18, no. 5, pp. 451–455, May 1998, doi: 10.1016/S0955-2219(97)00165-9.
- [69] S. Pai, “Calculation of Weibull strength Parameters and Batdorf Flow-Density Constants for Volume- and Surface-Flaw-Induced Fracture in Ceramics,” p. 34.
- [70] J. J. Masson and E. Bourgain, “Some guidelines for a consistent use of the Weibull statistics with ceramic fibres,” *Int J Fract*, vol. 55, no. 4, pp. 303–319, Jun. 1992, doi: 10.1007/BF00035188.

- [71] S. C. Cox, J. A. Thornby, G. J. Gibbons, M. A. Williams, and K. K. Mallick, “3D printing of porous hydroxyapatite scaffolds intended for use in bone tissue engineering applications,” *Materials Science and Engineering: C*, vol. 47, pp. 237–247, Feb. 2015, doi: 10.1016/j.msec.2014.11.024.
- [72] J.-W. Lee, Y.-H. Lee, H. Lee, Y.-H. Koh, and H.-E. Kim, “Improving mechanical properties of porous calcium phosphate scaffolds by constructing elongated gyroid structures using digital light processing,” *Ceramics International*, vol. 47, no. 3, pp. 3252–3258, Feb. 2021, doi: 10.1016/j.ceramint.2020.09.164.
- [73] H. Jin, Y. Zhuo, Y. Sun, H. Fu, and Z. Han, “Microstructure design and degradation performance in vitro of three-dimensional printed bioscaffold for bone tissue engineering,” *Advances in Mechanical Engineering*, vol. 11, no. 10, p. 168781401988378, Oct. 2019, doi: 10.1177/1687814019883784.
- [74] B. Huang, G. Caetano, C. Vyas, J. Blaker, C. Diver, and P. Bartolo, “Polymer-Ceramic Composite Scaffolds: The Effect of Hydroxyapatite and B-tri-Calcium Phosphate,” *Materials*, vol. 11, p. 129, Jan. 2018, doi: 10.3390/ma11010129.
- [75] C. Benaqqa, J. Chevalier, M. Saïdaoui, and G. Fantozzi, “Slow crack growth behaviour of hydroxyapatite ceramics,” *Biomaterials*, vol. 26, no. 31, pp. 6106–6112, Nov. 2005, doi: 10.1016/j.biomaterials.2005.03.031.
- [76] V. P. Orlovskii, V. S. Komlev, and S. M. Barinov, “Hydroxyapatite and Hydroxyapatite-Based Ceramics,” *Inorganic Materials*, vol. 38, no. 10, pp. 973–984, Oct. 2002, doi: 10.1023/A:1020585800572.
- [77] S. Dasgupta, S. Tarafder, A. Bandyopadhyay, and S. Bose, “Effect of grain size on mechanical, surface and biological properties of microwave sintered hydroxyapatite,” *Materials Science and Engineering C*, p. 9, 2013.
- [78] B. M. Moshtaghioun, D. Gomez-Garcia, A. Dominguez-Rodriguez, and Richard. I. Todd, “Grain size dependence of hardness and fracture toughness in pure near fully-dense boron carbide ceramics,” *Journal of the European Ceramic Society*, vol. 36, no. 7, pp. 1829–1834, Jun. 2016, doi: 10.1016/j.jeurceramsoc.2016.01.017.
- [79] J. A. Wollmershauser *et al.*, “An extended hardness limit in bulk nanoceramics,” *Acta Materialia*, vol. 69, pp. 9–16, May 2014, doi: 10.1016/j.actamat.2014.01.030.
- [80] S. Ramesh, C. Y. Tan, S. B. Bhaduri, and W. D. Teng, “Rapid densification of nanocrystalline hydroxyapatite for biomedical applications,” *Ceramics International*, vol. 33, no. 7, pp. 1363–1367, Sep. 2007, doi: 10.1016/j.ceramint.2006.05.009.
- [81] S. Bose, “Microwave-processed nanocrystalline hydroxyapatite: Simultaneous enhancement of mechanical and biological properties,” *Acta Biomaterialia*, p. 9, 2010.
- [82] J. Wang and L. L. Shaw, “Nanocrystalline hydroxyapatite with simultaneous enhancements in hardness and toughness,” *Biomaterials*, vol. 30, no. 34, pp. 6565–6572, Dec. 2009, doi: 10.1016/j.biomaterials.2009.08.048.
- [83] M. Prakasam, J. Locs, K. Salma-Ancane, D. Loca, A. Largeteau, and L. Berzina-Cimdina, “Fabrication, Properties and Applications of Dense Hydroxyapatite: A Review,” *Journal of Functional Biomaterials*, vol. 6, no. 4, pp. 1099–1140, Dec. 2015, doi: 10.3390/jfb6041099.
- [84] S. Pramanik, A. K. Agarwal, K. N. Rai, and A. Garg, “Development of high strength hydroxyapatite by solid-state-sintering process,” *Ceramics International*, vol. 33, no. 3, pp. 419–426, Apr. 2007, doi: 10.1016/j.ceramint.2005.10.025.

APPENDIX

Appendix A: Slurry Protocol

Appendix B: Gyroid File Generation

Appendix C: Compression Testing Protocol

Appendix A: 41 % Vol hydroxyapatite slurry mixing protocol

Author: Katherine Lopez Ambrosio

Objective:

Production of 15ml of 41%Vol hydroxyapatite slurries suitable for 3D printing.

Reagents:

Name		Acronym	Quantity	Brand
Tricalcium phosphate tribasic (Hydroxyapatite)	Ceramic	HAp	19.311 g	Macron fine chemicals
Diphenyl (2,4,6trimethylbenzoyl) phosphine oxide	Photoinitiator	TPO	0.036g	TCI America.
Solplus D540	Dispersant	D540	1.46ml	Lubrizol Advanced Materials Inc.
Ethylene glycol dimethacrylate	Monomer	EGDMA	7.5ml	Scientific Polymer Products Inc.

Materials and equipment:

- [1] Stainless steel spatula.
- [2] Laboratory scoopula.
- [1] 1ml Luer tip syringe.
- [NA] Planetary ball mill (PBM) brand: across international.
- [10g] Agate balls (weight ratio 2:1 HAp to agate balls)
- [1] Teflon jar of 50ml for planetary ball mill with chemical resistant O-ring.
- [1] Measuring paper.
- [1] 10 ml Graduated cylinder.
- [1] Benchtop Balance.
- [NA] Parafilm film or tape.
- [10ml] Plastic syringe.
- [1] PTFE Syringe stopper.
- [NA] Aluminum foil.
- [1] Metallic tongs

Acknowledgments before beginning the procedure:

- Use protective glasses, gloves and lab coat.
- Use the fume hood for the mixing and transferring procedure.
- This procedure is to produce 15ml of HAp slurry. However, Due to the electrosteric interaction of the HAp particles with the dispersant, the resultant volume of slurry is lower.
- The planetary ball mill is in the factory campus. In the setting of this machine zero count a cycle. So, if we need 15min of mixing in a 50% duty cycle, the PBM is programmed to work 2 cycles and to rest 2 cycles.

Procedure:

1. Use the weigh paper, graduated cylinder and, 1ml syringe to measure the photoinitiator TPO, the monomer of EDGMA and dispersant D540 respectively. Add all to the Teflon jar.
2. Place 10g of agate media (5 big balls and approximately 6 small balls) in the Teflon jar.
3. Set the O-ring in the cleavage of the Teflon jar. Close and seal the jar and lid with parafilm paper.
4. Install and lock the jar in the PBM. Assure that the jar is completely fastened. Mix the components for 30 minutes at 120rpm in a 50% duty cycle (3 cycles 5 min on, 5 min off).
5. Wait until step 4 finishes.
6. weigh 10g of HAp.
7. Remove the jar from the PBM and add the HAp in the solution. Mix the components with the spatula and seal the jar and lid with parafilm.
8. Fasten the jar in the PBM and set it at 300RPM for 2h in a 50% duty cycle (12 cycles of 5min on, 5min off).
9. Wait until step 8 finishes.
10. Weigh 5g of HAp.
11. Repeat step 7.
12. Fasten the jar in the PBM and set it at 320RPM for 2h in a 50% duty cycle (12 cycles of 5min on, 5min off).
13. Wait until step 11 finishes.
14. Weigh 4.311g of HAp
15. Repeat step 7.
16. Fasten the jar in the PBM and set it at 360RPM for 4h in a 50% duty cycle (12 cycles of 5min on, 5min off).

Next day to transfer the slurry to the syringes.

17. Open the jar. Collect the agate balls with the tongs and clean the walls of the jar with the spatula.
18. Mix the slurry manually for 5min.
19. Assure visually that the slurry does not show any clusters of HAp and that it is homogenous. If it is not homogenous mix manually for 5min more.
20. Transfer the slurry to the plastic syringe, close the tip of the syringe with the stopper. Wrap the syringe with aluminum foil.

Appendix B: Creating gyroid files for 3D printing

Author: Nelson Isaacson

Objective: Create a GCode file of a gyroid structure that can be printed on the Hyrel machines.

Materials:

- CAD file of sample
 - Must be .3mf, .amf, .ctm, .stl, or .obj
- Slicer software
 - Ultimaker Cura recommended
 - Other slicers may work, this method is confirmed to work with Cura.
- GCode Template file
 - Located on SharePoint
 - Template file must match intended Hyrel machine (Hydra, ESR, SR)
- Text editor
 - Notepad++ recommended

Preparation:

1. Run the slicer software.
2. Import the CAD file into the slicer.
3. In print settings, set the following parameters:
 - a. Layer Height: 0.2 mm
 - b. Line Width: 0.413 mm
 - i. Dependent on nozzle size. A 22g nozzle is 0.413 mm in diameter.
 - c. Wall Thickness: 0.0 mm
 - d. Top/Bottom Thickness: 0.0 mm
 - e. Infill Pattern: Gyroid
 - f. Infill Density: 20%, 30%, or 40%
 - i. This will generate 80%, 70%, or 60% porous gyroids, respectively.
4. Select “Slice” to generate the initial GCode.
5. Select “Save to Disk” or “Save to File” (depending on slicer and slicer version) and save the file in an accessible location.
6. Open both the generated GCode file and the GCode template file in Notepad++.
7. In the generated GCode file, copy the code starting with

M107

M204 S500

M205 X8 Y8

And ending with

M140 S0

M204 S1500

M205 X6 Y6

M107

The beginning section starts ~line 40, the final section ends near the end of the document. This will be several thousand lines of code.

8. Paste the code into the Hyrel template file after the BEGIN ALTERED CODE line.
9. Save the GCode file with a new name.
10. The file is now ready to be loaded into REPETREL.

Notes:

1. This method is confirmed to work with Ultimaker Cura.
2. This method can be used with any CAD design, it is not limited to cubes or other simple geometry.
3. Print parameters such as LED power, steps/um, etc., must be controlled via REPETREL, this method only generates the print moves.
4. A video tutorial is available on the SharePoint.

Appendix C: Compression testing of porous ceramic scaffolds.

Author: Nelson Isaacson

Objective: Perform compression tests of porous ceramic scaffolds to determine mechanical responses.

Materials:

- Test Sample(s)
- Latex/lab gloves
- Safety Glasses
- Tweezers
- Calipers
- High-grit (1000+) sandpaper
- Kim wipes
- Individual sample bags (if post-test SEM is desired)
- Tinius Olsen H1KS Benchtop Tester (or equivalent)
- Compression platens for benchtop tester

Sample Preparation:

11. Measure the height of the test sample in several spots to determine if the test planes are parallel.
12. Place the sandpaper grit-side up on a work surface.
13. While wearing gloves and safety glasses, begin sanding the first desired test surface by holding the sample and lightly applying pressure to the sandpaper while moving the sample back and forth, taking care to apply even pressure across the surface.
14. After a few passes along the sandpaper, repeat step 3 for the other side.
15. Measure the height of the sample in several places.
16. If the height varies, repeat steps 3-5. If the height is consistent across the tested locations, move to the next section. **It is critical that the surfaces that are being loaded are as parallel as possible.**

Test Preparation:

1. Ensure that the software key is plugged into the back of the test computer. It looks like a USB drive and is labeled “software key, not a USB drive”.
2. Turn on the H1KS and sign into the computer using the test admin sign-in information.
3. Select “Navigator” on the desktop to open the test software and link the computer to the H1KS.
4. Select “Edit” in the upper-left corner to open the Test Settings menu.

5. If replicating previously used parameters, select the test name from the drop-down menu in the upper-right corner of the Test Settings menu.
6. To develop a new test, there are four sub-menus to go through. The following contains settings from the test standard as of January 2021.
 - a. "Parameters"
 - i. Test Type: Compression from Position
 - ii. Specimen Shape: Flat
 - iii. Specimen Height: Nominal height of specimens
 - b. "Machine Control"
 - i. Position Rate: 0.1 mm/min
 - ii. End Condition: 75% DropOff
 - c. "Reporting"
 - i. "Printout"
 1. Double click in the table to edit the saved information
 2. Create columns for the following:
 - a. Sample ID
 - b. Sample No.
 - c. Area
 - d. Force
 - e. Ultimate Stress
 - f. Modulus
 - ii. "ASCII"
 1. Set the save file path in the first entry field.
 2. Select "Delimited fields"
 - a. Delimiter: comma
 3. Select "Export with Summary"
 4. Select "Include Header"
 5. Repeat 6.c.i.2 to create output columns
 - d. "Graphing"
 - i. "Printout"
 1. Graph parameters are set here
 2. Set Y-Axis as Stress in MPa
 3. Set X-Axis as Strain in m/m
 4. Either select "Auto Scale" for both axes or enter desired axes scale.
 - ii. "ASCII"
 1. Set the save file path in the first entry field.
 2. Select "Delimited fields"
 - a. Delimiter: comma
 3. Set "Number of points" as "Actual"
 4. Create output columns for Stress (in MPa) and Strain (in m/m)
 - e. Select "Save As" in the upper-left corner and save the test parameters with the desired name.

- i. Recommended to be descriptive, i.e., “0_1 mm_min Gyroid Cube Compression”
- f. Click “Done” in the Test Settings menu

Test Procedure:

Safety glasses **MUST** be worn during material testing. The ceramic scaffolds may shatter during testing and eject fragments that can strike the operator. These fragments are unlikely to damage skin but can easily damage unprotected eyes. If, at any time, there is a presented danger, immediately turn off the H1KS by depressing the red Emergency Stop button near the power switch.

1. In the Test Navigator software, select “Test” in the upper-left ribbon menu.
 - a. You should see an empty graph on the screen.
2. In the upper-right menu, enter the “Lot” and “Operator” information.
 - a. This can be used to track when the scaffolds were made and who performed the test. Examples:
 - i. Lot: 20210116
 - ii. Operator: Nelson Isaacson
3. On the H1KS, lower the test platen by pressing and holding the down arrow on the H1KS interface.
4. Using tweezers, place the test sample in the center of the bottom platen.
5. Press “F1 zero force” on the H1KS.
6. Raise the test platen into position by pressing and holding the up arrow on the H1KS interface.
 - a. Raise the platen until the test sample is very lightly contacting the upper platen. The “Force” readout on the H1KS screen will help verify the contact. The force should be less than 1 N.
 - b. Briefly press the down arrow to lower the sample from contact. The Force readout should display 0 N.
7. Press “F1 zero force” and “F2 zero ext” on the H1KS.
8. In Test Navigator, enter Sample, Sample No, Width, and Thickness in the upper-right.
 - a. Recommended format:
 - i. Sample: for a 60% porous gyroid tested in the normal direction, identify the sample as 60N
 - ii. Sample No: Test batch and specific sample. For example, the fourth sample in the second set of measurements would be 2.4
 - iii. This combines to identify the specific samples, such as 60N2.4
9. Select “Test Now” in the upper-right to begin the test.
 - a. To cancel the test, click “Abort” in the upper-right.

10. The test will take several minutes to complete. The H1KS will begin emitting beeping sounds to indicate that the crosshead is moving. The graph on the screen will update in real-time.
11. Once the test finishes, Test Navigator will provide a list of the recorded data.
 - a. Select “Accept” or “Discard” if you’d like to keep the data or discard it, respectively.
12. Test Navigator will display a prompt to return the crosshead. Click “OK” to do so.
13. Remove the sample from the platen
 - a. Recommended to save larger pieces for potential SEM imaging.
 - i. This can be done with the small plastic bags near the H1KS.
14. Clean the platens using a Kim wipe.
15. Update the sample number in Test Navigator and repeat steps 3-14 for your next sample.

Saving Results:

1. To save a specific graph, select the sample from the list on the bottom of the screen.
 - a. Select the arrow next to “Print” in the upper-left of the screen and select “to File (BMP)”
 - b. Enter a name for the graph and save to your results folder on the computer.
2. To save specific sample results, select the sample from the list on the bottom of the screen.
 - a. Right-click and select “Export Selected”
 - b. This will save a .csv to the file path selected earlier.
3. To save all of the results to one file, right click in the bottom list and select “Export All”
4. **WARNING:** Selecting “Export Summary” will **REMOVE** the results from being accessible.
5. Use a jump drive or other USB devices to retrieve the files from the computer.

Ensure that the work area is cleaned following testing.

Notes:

1. Final failure was determined to be 75% stress drop from the peak stress. No relevant stress-strain data (such as significant amounts of self-reinforcement) was found after a 65% stress drop in earlier tests. Continuing the compression test past this point is unlikely to yield meaningful data and risks damage to the machine.
2. Failing to properly clean the H1KS can cause subsequent tests to provide faulty data.